Measurement of Tagged Deep Inelastic Scattering (TDIS)

May 26, 2014

A. Camsonne, D. Gaskell, D. Higinbotham, C. E. Keppel, W. Melnitchouk, C. Weiss, B. Wojtsekhowski
JEFFERSON LAB

R. Holt, P. Reimer
ARGONNE NATIONAL LAB

M.E. Christy, N. Kalantarians, M. Kohl, P. Monaghan
HAMPTON UNIVERSITY

P. King, J. Roche
OHIO UNIVERSITY

J. Dunne, D. Dutta, A. Narayan,
L. Ndukum, A. Subedi, and L. Ye
MISSISSIPPI STATE UNIVERSITY

S. Bueltmann, C. Hyde, S. Kuhn, L. Weinstein
OLD DOMINION UNIVERSITY

J. R. M. Annand
UNIVERSITY OF GLASGOW

J.-C. Peng
UNIVERSITY OF ILLINOIS AT URBANA CHAMPAIGN

G. Cates, K. Gnanvo, R. Lindgren, N. Liyanage, J. Zhang
UNIVERSITY OF VIRGINIA

T. Averett, K. Griffeon
COLLEGE OF WILLIAM AND MARY

T. Hobbs, T. Londergan
INDIANA UNIVERSITY

Xiaodong Jiang
LOS ALAMOS NATIONAL LABORATORY

THE SBS COLLABORATION

Abstract

We propose to investigate tagged deep inelastic scattering (TDIS), by measuring high W^2, Q^2 electrons scattered from hydrogen and deuterium targets in coincidence with low momentum recoiling protons (or pairs of protons in the case of the deuteron). This is a pioneering experiment that will measure the component of the nucleon structure function related to bound objects within the nucleon, tagging for example the pion as the target in proton to pion fluctuations. It will thereby provide a probe of the meson cloud component in the nucleon, and directly measure fracture functions. At (extrapolated) low values of t, this approach will be specifically sensitive to the pion structure function via the Sullivan process.

The experiment utilizes the Hall A Super BigBite spectrometer for electron detection, in conjunction with the thin target, solenoid and GEM-based radial time projection chamber approach that was realized in experiments such as BONUS and eg6 for low momentum spectator tagging. These combined systems, in combination with the CEBAF high current CW beam, leverage the high luminosity and unique considerations required to access the proposed physics. The low momentum tagging technique will reduce backgrounds from both experimental and theoretically competing processes, enhancing isolation of the electron-pion events.

Contents

1   Physics Motivation

The concept of a composite nucleon structure may be tracked as far back as 1933 to the discovery of the anomalous magnetic moment of the proton [1]. This was explicitly formulated by Fermi and Marshall who noted in a 1947 paper [2] that experimental evidence pointed to the nucleon existing approximately 20% of the time in a virtual meson-nucleon state. The virtual meson "cloud" of the nucleon plays an important role in the understanding of the nucleon-nucleon interaction and the pion cloud in particular has always been considered critical to understanding the nucleon's long-range structure. At shorter ranges, the role of mesons in electron-nucleon deep inelastic scattering (DIS) have also been investigated. In 1972 Sullivan [3] suggested that some fraction of the nucleon's anti-quark sea distribution may be associated with this pion content of the nucleon. For many decades these and numerous other theories that describe and/or utilize the meson cloud of the nucleon have advanced significantly (see [4, 5, 6] for some review). From partially conserved axial current to the success of chiral quark models, it is considered known that the nucleon has an associated meson cloud. In very stark contrast to the substantial body of theory associated with the cloud, however, experimental results remain few and far between. In a 1983 paper, Thomas commented that "...it is rather disturbing that no one has yet provided direct experimental evidence of a pionic component in the nucleon" [7]. Even with some results available from Drell-Yan experiments at Fermilab, W production at RHIC, and diffractive DIS at HERA and COMPASS, all discussed below, the "disturbing" situation is not much different today.

The physics motivation for this experiment is, then, basically this: to pioneer a measurement technique probing the elusive mesonic content of the nucleon structure function. To motivate this measurement, we start with a description of the kinematics and predictions for the mesonic component of the nucleon structure function, then turn to the fracture function formalism which provides a QCD framework for description of this component in the target fragmentation region, and end with an extension of the expected results to extract the pion structure function via the Sullivan process. These sections follow.

1.1   Tagged Deep Inelastic Scattering (TDIS)

In specific regions of kinematics, the observation of low-momentum recoil protons in the semi-inclusive reaction $eN \rightarrow eNX$ can reveal features associated with correlated $q\bar{q}$ pairs in the nucleon, sometimes referred to as the nucleon's "pion cloud". In particular, at low values of the four-momentum transfer squared $t \equiv k^2 = (p - p')^2$, where p and p' are the initial and final nucleon four-momenta, the cross section displays behavior characteristic of pion pole dominance. Here, the contributions from the exchange of non-pseudoscalar quantum numbers ($J^P = 0^-$), such as the vector ρ and ω mesons, is suppressed. Furthermore, the direct fragmentation of the scattered quark, or spectator "diquark" system that remains after a quark is pulled out of the nucleon, generally produces a considerably more flat t dependence that is qualitatively different from that arising from the pion pole.

Here we review the predictions of pion cloud models for contributions to the structure functions of the nucleon, firstly for the inclusive DIS case, and then to the semi-inclusive

4

cross sections, which we study as a function of several kinematic variables.

1.1.1 Meson cloud contributions to inclusive DIS

As pointed out by Sullivan [3], the contribution to the inclusive F_2 structure function of the nucleon from scattering off a virtual pion emitted from the nucleon can be written as

$$F_2^{(\pi N)}(x) = \int_x^1 dz \, f_{\pi N}(z) \, F_{2\pi}\left(\frac{x}{z}\right), \tag{1}$$

where $z = k^+/p^+$ is the light-cone momentum fraction of the initial nucleon carried by the interacting pion. In the infinite momentum frame this coincides with the longitudinal momentum fraction, while in the rest frame of the target nucleon, which we will use in the following, z is expressed as $z = (k_0 + |\mathbf{k}| \cos\theta)/M$, where M is the mass of the nucleon, $k_0 = M - \sqrt{M^2 + \mathbf{k}^2}$ is the pion energy, and θ is the angle between the vector $\mathbf{k}$ and the z-axis (which is equal to the angle between the recoil proton momentum $\mathbf{p}'$ and the photon direction). For ease of notation, we also suppress the explicit dependence of the structure functions on the scale Q^2.

The function $f_{\pi N}(z)$ gives the light-cone momentum distribution of pions in the nucleon,

$$f_{\pi N}(z) = c_I \frac{g_{\pi NN}^2}{16\pi^2} \int_0^\infty \frac{dk_\perp^2}{(1-z) \, z} \frac{G_{\pi N}^2}{(M^2 - s_{\pi N})^2} \left(\frac{k_\perp^2 + z^2 M^2}{1 - z}\right), \tag{2}$$

where $k_\perp$ is the transverse momentum of the pion, $g_{\pi NN}$ is the πNN coupling constant, and the isospin factor $c_I = 1$ for π^0 ($p \to p\pi^0$ or $n \to n\pi^0$) and $c_I = 2$ for $\pi^\pm$ ($p \to n\pi^+$ or $n \to p\pi^-$). The function $G_{\pi N}$ parametrizes the momentum dependence of the πNN vertex function, which, due to the finite size of the nucleon, suppresses contributions from large-$|\mathbf{k}|$ configurations. Similar expressions (though somewhat more involved) can be written for other contributions, such as from ρ mesons or with Δ baryons in the final state. However, because of the small mass of the pion, the πN configuration is expected to be the dominant one. In Eq. (2) the variable $s_{\pi N} = (k_\perp^2 + m_\pi^2)/z + (k_\perp^2 + M^2)/(1-z)$ represents the total squared center of mass energy of the intermediate πN system, and is related to the pion virtuality t by $t - m_\pi^2 = z(M^2 - s_{\pi N})$.

The form factor $G_{\pi N}$ (or more generally G_{MN} for a meson M) can be constrained by comparing the meson cloud contributions with data on inclusive $pp \to nX$ scattering, as performed by Holtmann *et al.* [10]. For the purpose of this proposal, we use the parametric form

$$G_{\pi N} = \exp\left[(M^2 - s_{\pi N})/\Lambda^2\right], \tag{3}$$

where Λ is the form factor cutoff parameter. (Note that in Ref. [10] a parametrization of the form $\exp[(M^2 - s_{\pi N})/2\Lambda^2]$ is used, so that the corresponding cutoffs there are smaller by a factor of $\sqrt{2}$.) An illustration of the typical spectra for the differential cross section $E d^3\sigma/d^3p'$ in the $pp \to nX$ reaction arising from π and ρ exchange is shown in Fig. 1 as a function of the light-cone momentum fraction $\bar{z} \equiv 1 - z$ carried by the final nucleon, for two values of the transverse momentum $k_\perp$. For small $k_\perp$ the π exchange contribution clearly dominates at all $\bar{z}$, while at larger momenta the contributions from heavier mesons such as the ρ become more important.
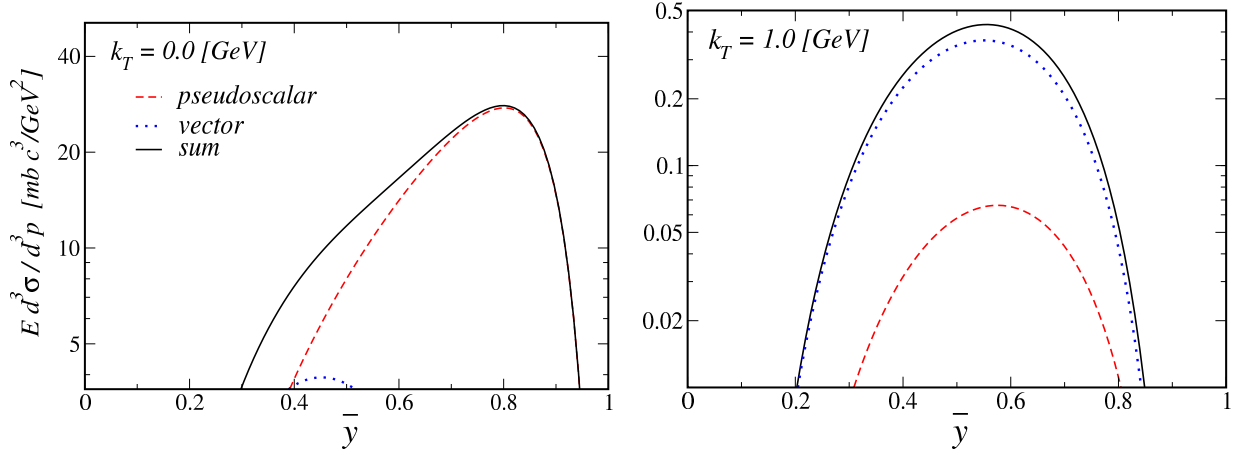
Figure 1: Typical spectra for the differential cross section $Ed^3\sigma/d^3p'$ in the $pp \to nX$ reaction for transverse momentum $k_\perp = 0$ (left panel) and $k_\perp = 1$ GeV (right panel), as a function of the light-cone momentum fraction $\bar{z} \equiv 1 - z$. The pseudoscalar π (red dashed lines) and vector ρ (blue dotted lines) contributions, and their sum (black solid lines), are indicated explicitly.
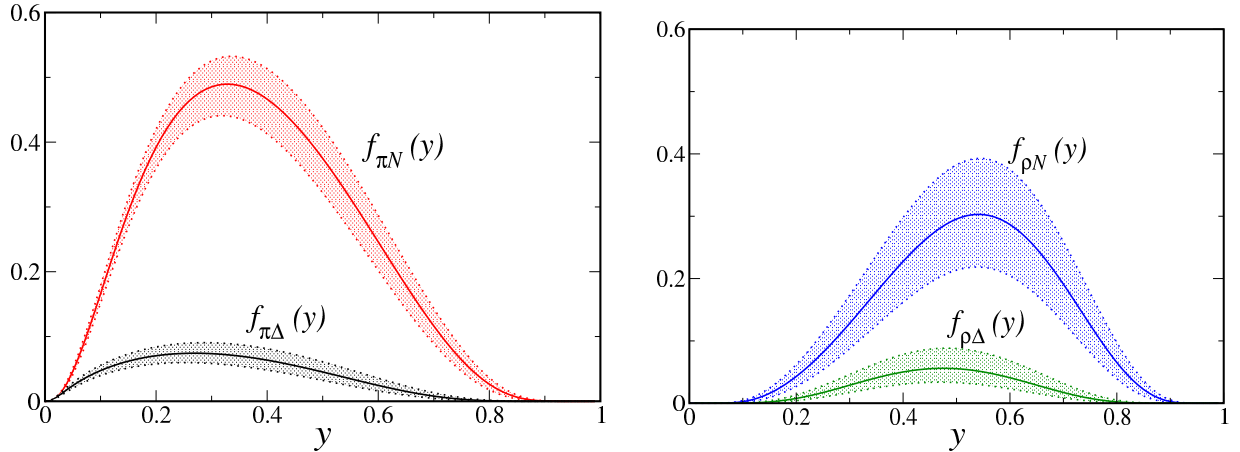

Figure 2: Light-cone momentum distributions of the pion, $f_{\pi N}$ and $f_{\pi\Delta}$ (left panel) and the ρ meson, $f_{\rho N}$ and $f_{\rho\Delta}$ (right panel), as a function of the meson light-cone momentum fraction z. The error bands correspond to the cutoff parameter ranges as given in the text.
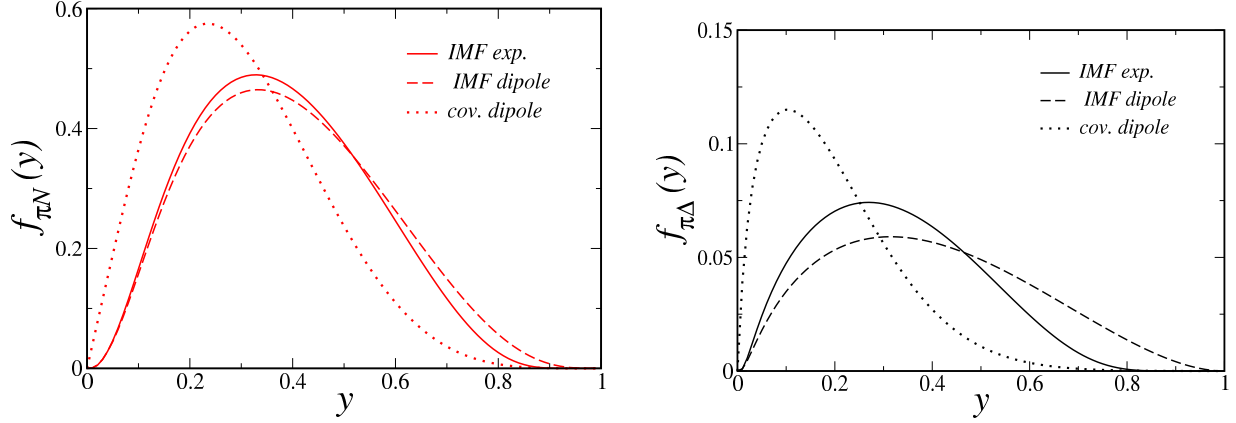
Figure 3: Light-cone momentum distributions for the πN (left panel) and $\pi\Delta$ (right panel) intermediate states, for several different functional forms of the form factor G in Eq. (2): "IMF" refers to s-dependent forms such as in Eq. (3), while "cov" denotes a form factor that depends only on the variable t.

Using the cutoff parameters constrained by the inclusive hadronic $pp \to nX$ data, which were found in Ref. [10] to be $\Lambda_{\pi N} = \Lambda_{\rho N} = 1.56 \pm 0.07$ GeV and $\Lambda_{\pi\Delta} = \Lambda_{\rho\Delta} = 1.39 \pm 0.07$ GeV, the light-cone momentum distributions $f(z)$ are shown in Fig. 2. The principal model uncertainty in these results comes from the ultraviolet regulator G used to truncate the $k_\perp$ integrations in the distribution functions. Various functional forms have been advocated in the literature aside from the s-dependent exponential form factor in Eq. (3), and we compare several of these, including s- and t-dependent dipole forms) in Fig. 3. For the s- and t-dependent forms in particular, the differences are noticeable mostly at small values of z, where the t-dependent parametrization (of the form $G \sim 1/(t-\Lambda^2)^2$) tends to give somewhat larger distributions that are peaked at smaller z, compared with the s-dependent form, which tend to be broader.

Convoluting the light-cone distributions with the structure function of the meson as in Eq. (1), the resulting contributions from the πN and ρN intermediate states to the inclusive F_2 structure function of the proton is illustrated in Fig. 4. For the meson structure function we use the parametrization from GRV, and assume that $F_{2\pi}(x) \approx F_{2\rho}(x)$. The results are plotted for fixed values of the scattering angle of the final state electron θ_e, which determines the Q^2 dependence of the contribution at a given x. For angles between $\theta_e = 15°$ and $40°$ the Q^2 dependence is rather negligible due to the mild Q^2 dependence of the meson structure function. For the fully integrated results of Fig. 4, the model uncertainties are greatest for the lowest accessible values of $x \sim 0.05$; depending upon choice of the phenomenological cutoff parameter Λ, the π contribution to F_2 can either be comparable to that of the ρ, or even larger at high values of x (where the calculation is also less reliable).
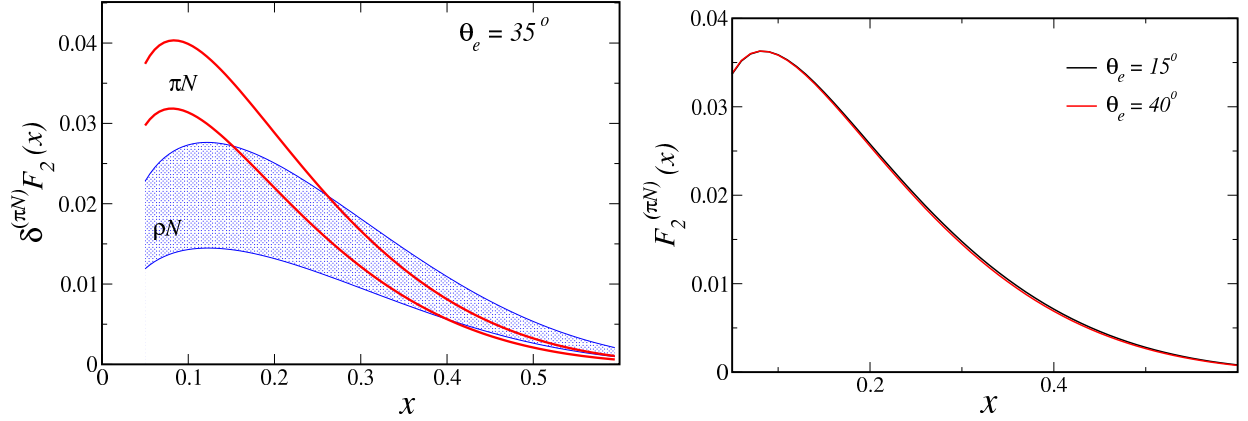
Figure 4: Contributions from πN and ρN intermediate states to the inclusive F_2 structure function of the proton for fixed electron scattering angle $\theta_e = 35°$ (left panel), and at two different angles, $\theta_e = 15°$ and $40°$ (right panel) for the πN contributions.

1.1.2 Tagged Structure Functions

While the inclusive reactions requires integration of the pion momentum over all possible values, detecting the recoil proton in the final state allows one to dissect the internal structure with significantly more detail and increase the sensitivity to the dynamics of the meson exchange reaction. In general, we will be interested in the relative contributions of the semi-inclusive reaction with respect to the inclusive process. In practice, the semi-inclusive structure function will be given by the unintegrated product

$$F_2^{(\pi N)}(x, z, k_\perp) = f_{\pi N}(z, k_\perp)\, F_{2\pi}\left(\frac{x}{z}\right), \tag{4}$$

where the unintegrated distribution function $f_{\pi N}(z, k_\perp)$ is defined by

$$f_{\pi N}(z) = \frac{1}{M^2} \int_0^\infty dk_\perp^2\, f_{\pi N}(z, k_\perp^2). \tag{5}$$

The dependence of the tagged structure functions on the kinematical variables that are measured experimentally can be studied by relating the magnitude of the 3-momentum $\mathbf{k}$ of the exchanged pion in the target rest frame to the pion's transverse momentum $k_\perp$ and light-cone fraction z,

$$\mathbf{k}^2 = k_\perp^2 + \frac{[k_\perp^2 + (1 - [1 - z]^2)M^2]^2}{4M^2(1 - z)^2}. \tag{6}$$

Experimentally, the quantities most readily measured are the momentum of the produced proton, $\mathbf{p}'$, which in the rest frame is $\mathbf{p}' = -\mathbf{k}$, and the scattering angle $\theta_{p'} = \theta$ of the proton with respect to the virtual photon direction. In the limit $k_\perp^2 = 0$, the magnitude of $\mathbf{k}$ becomes

$$|\mathbf{k}|_{k_\perp^2 = 0} = \frac{zM}{2}\left(\frac{2 - z}{1 - z}\right), \tag{7}$$

which imposes the restriction $z \lesssim |\mathbf{k}|/M$. This relation is illustrated in Fig. 5 for values of z up to 0.2.
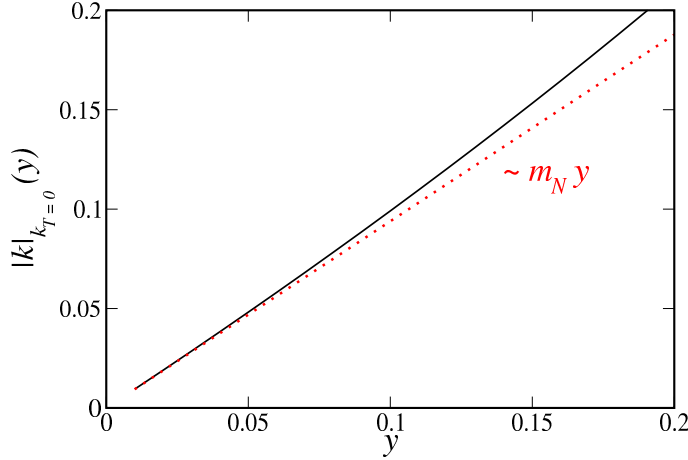
8

Figure 5: Pion momentum $|\mathbf{k}|$ as a function of the light-cone fraction z for $k_\perp = 0$ (black solid). The linear approximation $\sim zM$ (red dotted) is shown for comparison.

The kinematic restrictions on $|\mathbf{k}|$ for a given z can also be illustrated by considering the unintegrated light-cone distribution functions as a function of the variable t. This is relevant since one way of identifying the pion exchange mechanism is through its characteristic t dependence, which is pronounced near the pion pole at $t = +m_\pi^2$. The production of a physical proton (or Δ baryon) in the final state restricts the maximum value of t, however (corresponding to the minimum transverse momentum, $k_\perp = 0$), to

$$t_{\min}^N = -\frac{M^2 z^2}{1-z}, \qquad t_{\min}^\Delta = -\frac{(M_\Delta^2 - (1-z)M^2)\,z}{1-z}, \tag{8}$$

for nucleon N and Δ final states, respectively. Implementing these limits, the t-dependence of the distributions for π exchange with a nucleon or Δ recoil is illustrated in Fig. 6. Note that at the larger z value there is a considerable gap between the values of t at which Δ production is possible compared with N production.

Experimentally, the semi-inclusive cross sections will be measured in specific bins of recoil proton momentum $|\mathbf{p}'| = |\mathbf{k}|$ and scattering angle $\theta_{p'}$ (or equivalently z and $k_\perp$). We therefore define the partially integrated semi-inclusive structure function $F_2^{(\pi N)}(x, \Delta z, \Delta k_\perp^2)$,

$$F_2^{(\pi N)}(x, \Delta z, \Delta k_\perp^2) = \frac{1}{M^2} \int_{\Delta z} \int_{\Delta k_\perp^2} f_{\pi N}(z, k_\perp)\, F_{2\pi}\!\left(\frac{x}{z}\right), \tag{9}$$

integrated over the range $\Delta z = [z_{\min}, z_{\max}]$ and $\Delta k_\perp^2 = [k_{\perp\min}^2, k_{\perp\max}^2]$. Alternatively, one can define an analogous semi-inclusive structure function integrated over other variables, such as $|\mathbf{k}|$ and $\theta_{p'}$, by $F_2^{(\pi N)}(x, \Delta|\mathbf{k}|, \Delta\theta_{p'})$. The proposed experiment will probe the ranges of kinematics $0.05 \lesssim z \lesssim 0.2$ and $60 \lesssim |\mathbf{k}| \lesssim 400$ MeV, and angles $30 \lesssim \theta_{p'} \lesssim 160°$, with x in the vicinity of $x \sim 0.05 - 0.2$.

Fig. 7 shows the semi-inclusive structure functions $F_2^{(MN)}(|\mathbf{k}|; \Delta x, \Delta\theta_{p'})$ for $p \to \pi^0\, p$ and $p \to \rho^0\, p$, as a function of the momentum $|\mathbf{k}|$, integrated over x between 0 and 0.6,
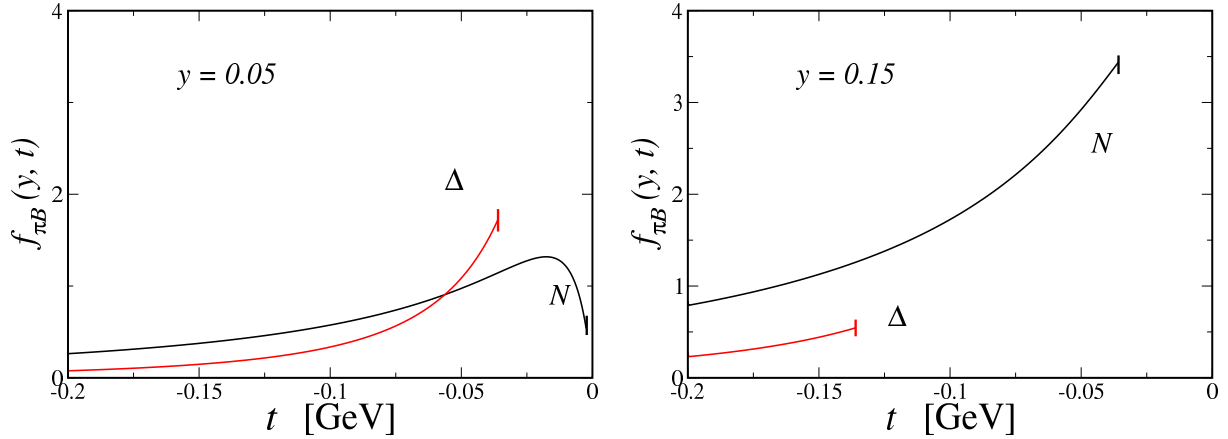
9

Figure 6: Unintegrated light-cone distribution functions for πN (black solid) and $\pi \Delta$ (red solid) states as a function of t, for fixed values of $z = 0.05$ (left) and $z = 0.15$ (right).

and over all angles $\theta_{p'}$ from 0 to π. The ρ contribution is clearly suppressed relative to the pion contribution. The structure functions rise with increasing $|\mathbf{k}|$ in the experimentally accessible region $|\mathbf{k}| \lesssim 0.5$ GeV. At larger momenta the effects of the meson–nucleon form factors become more important, which suppress the contributions from high-$|\mathbf{k}|$ tails of the distributions. The peak in the π distribution occurs at $|\mathbf{k}| \approx 0.6$ GeV, while the ρ distribution peaks at higher momenta, $|\mathbf{k}| \approx 1.2$ GeV, and has a slower fall-off with $|\mathbf{k}|$. The effect of the pion–nucleon form factors are also illustrated in Fig. 7, where the semi-inclusive structure functions are shown as a function of x, integrated over the momentum range $\Delta|\mathbf{k}| = [60, 250]$ MeV. The results with the the s-dependent (IMF) exponential and dipole form factors are compared with the t-dependent dipole form factor, as well as with the calculation without any form factor suppression of the ultraviolet contributions. As expected, the form factor dependence is relatively mild in this momentum interval, and it is only for larger momenta ($|\mathbf{k}| \gtrsim 0.5$ GeV) that the form factor model becomes significant.

The dependence of the semi-inclusive structure function $F_2^{(\pi N)}(x, \Delta k, \Delta \theta_{p'})$ on the pion structure function parametrization are shown in Fig. 8 as a function of x, integrated over the momentum range $\Delta|\mathbf{k}| = [60, 250]$ MeV and angular range $\Delta \theta_{p'} = [30°, 180°]$. The results with the GRV parametrization [18] of the pion parton distribution functions are compared with those using the MRS parametrization [19] with different amounts of sea, ranging from 10% to 20%. The pion structure function is relatively well constrained from pion–nucleon Drell-Yan data at Fermilab at intermediate and large values of x, but is not as well determined at small x values. Nevertheless, the variation in the computed semi-inclusive proton structure function from uncertainties in the pion distribution functions is very small, and considerably smaller than the uncertainties from the pion–nucleon vertex form factor dependence.

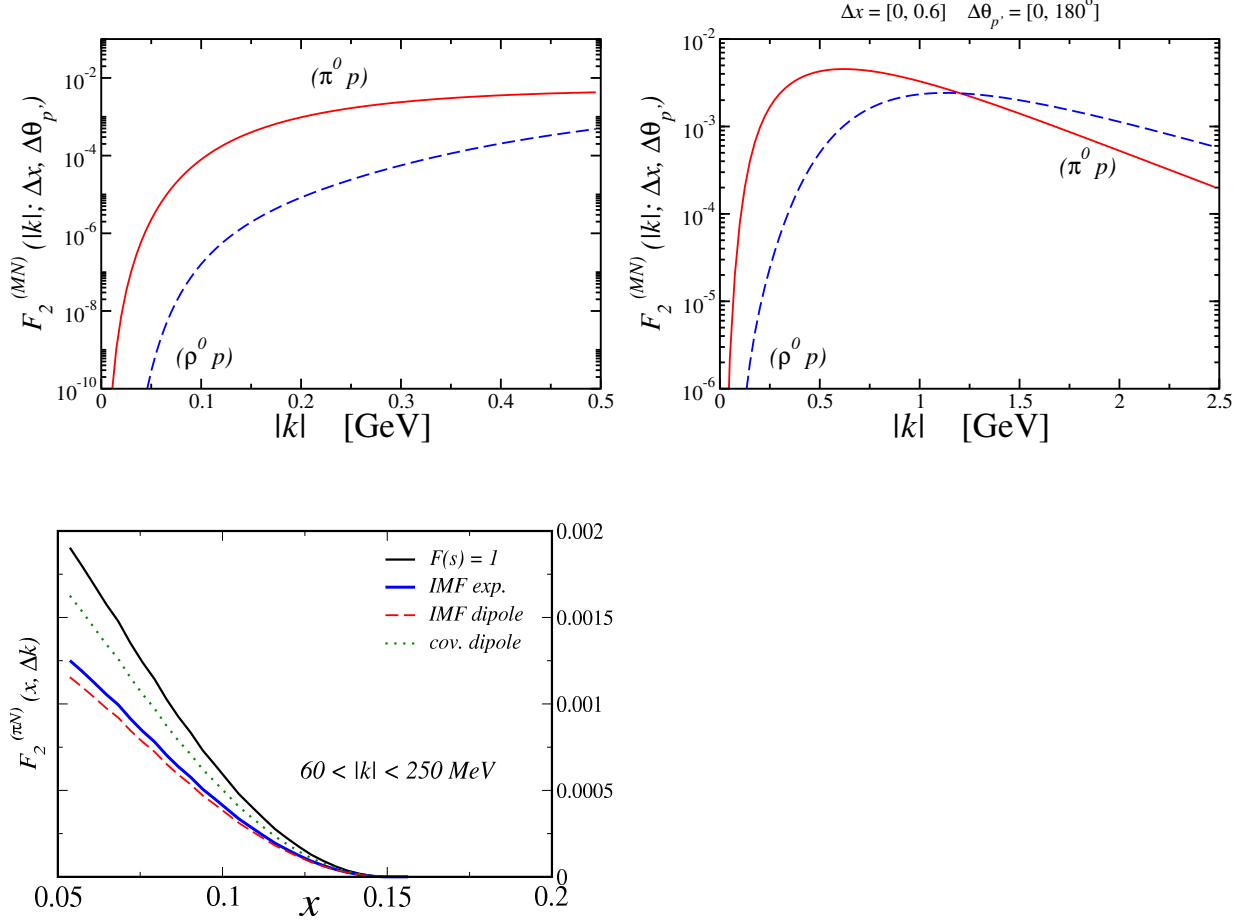Description of Fig. 9.

Description of Fig. 10.

Figure 7: (Top panels) Semi-inclusive structure functions $F_2^{(MN)}(|\mathbf{k}|; \Delta x, \Delta\theta_{p'})$ for the $p \to M\, p$ process, with $M = \pi^0$ (red solid) and $M = \rho^0$ (blue dashed), as a function of the recoil proton momentum $|\mathbf{k}|$, integrated over $\Delta = [0, 0.6]$ and all angles $\theta_{p'}$. The top left panel shows the function over the experimentally accessible range for $|\mathbf{k}|$ up to 0.5 GeV, while the top right panel shows the extended range up to $|\mathbf{k}| = 2.5$ GeV. (Bottom panel) Semi-inclusive structure function $F_2^{(\pi N)}(x; \Delta|\mathbf{k}|, \Delta\theta_{p'})$ as a function of x, integrated over the momentum range $\Delta|\mathbf{k}| = [60, 250]$ MeV. The results with the s-dependent (IMF) exponential (blue solid) and dipole (red dashed) form factors are compared with the t-dependent (covariant) dipole form factor (green dotted), and with no form factor (black solid).

11
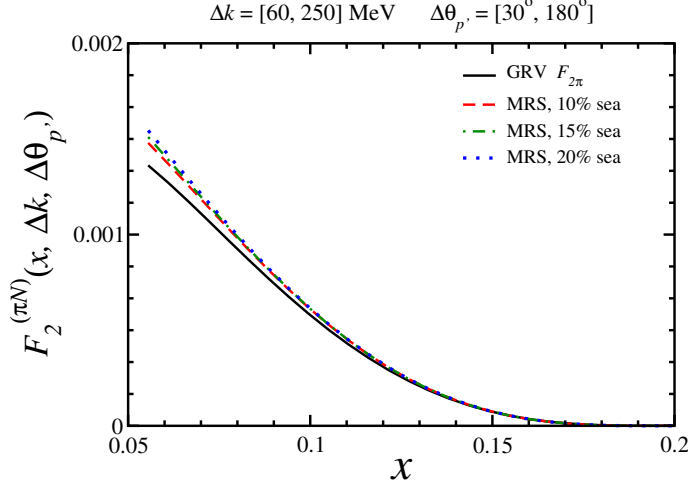
Figure 8: Semi-inclusive structure function $F_2^{(\pi N)}(x, \Delta k, \Delta\theta_{p'})$ for the $p \to \pi^0 p$ process, integrated over the momentum range $\Delta|\mathbf{k}| = [60, 250]$ MeV and angular range $\Delta\theta_{p'} = [30°, 180°]$. The results with the GRV [18] (black solid) parametrization of the pion structure function are compared with those using the MRS [19] fit with different amounts of sea, 10% (red dashed), 15% (green dot-dashed) and 20% (blue dotted).
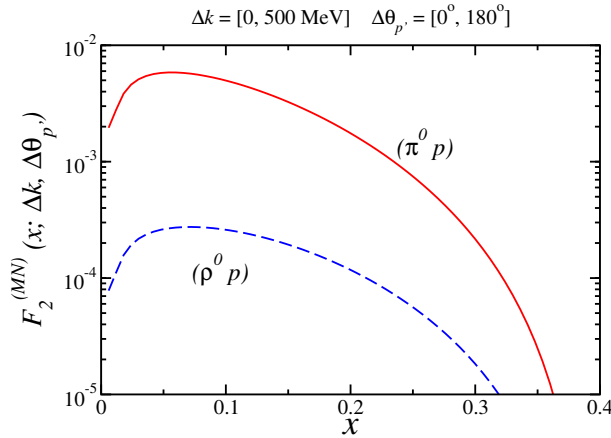
Figure 9: x dependence of the semi-inclusive structure function $F_2^{(MN)}(x, \Delta k, \Delta\theta_{p'})$ for $p \to \pi^0 p$ (red solid) and $p \to \rho^0 p$ (blue dashed), integrated over the momentum range $\Delta|\mathbf{k}| = [0, 500]$ MeV and over all angles $\theta_{p'}$.

12

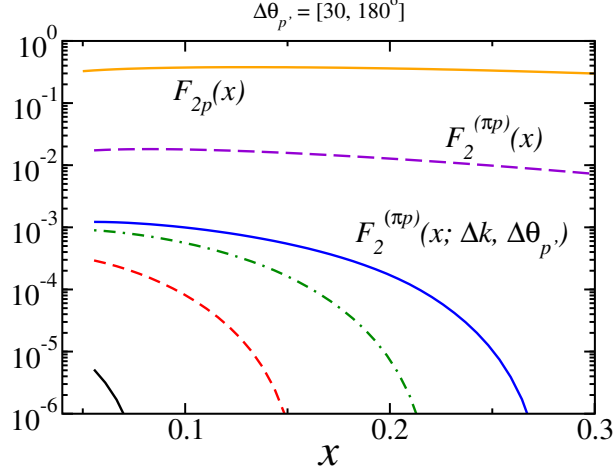Figure 10: x dependence of the semi-inclusive structure function $F_2^{(\pi p)}(x, \Delta k, \Delta\theta_{p'})$ ... ... For comparison, the total integrated πp contribution $F_2^{(\pi p)}$ to the inclusive proton structure function is shown (violed dashed), as is the total inclusive F_{2p} structure function (orange solid).
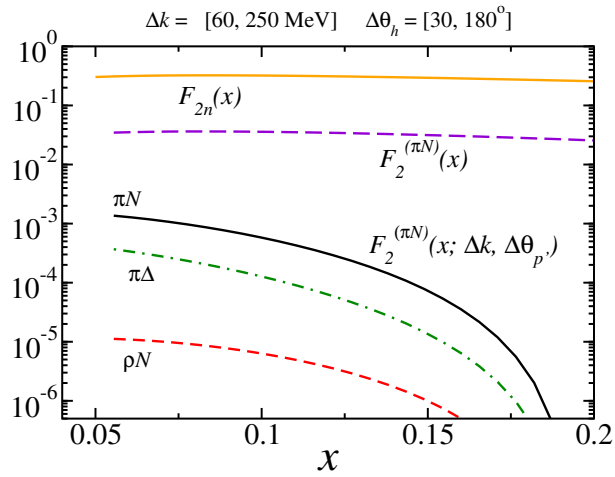

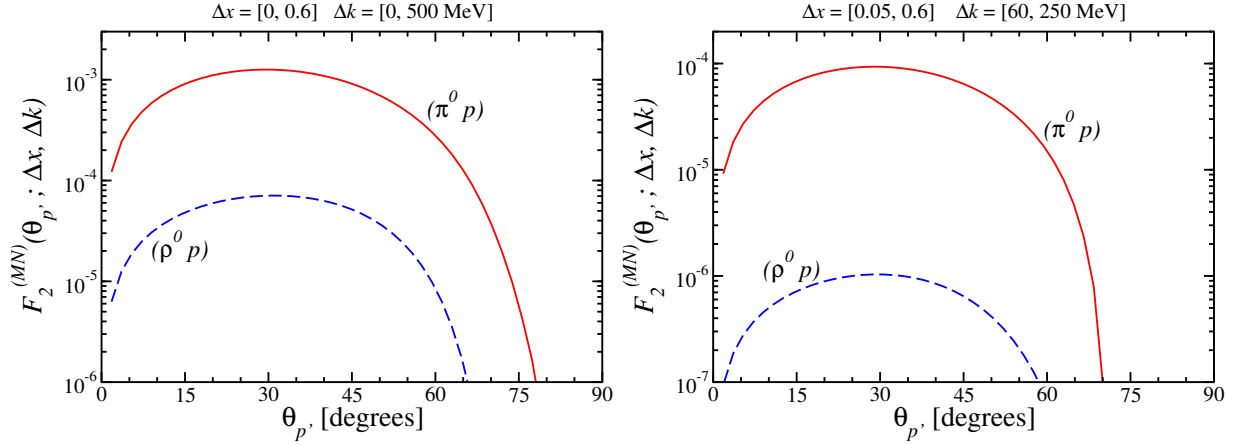Figure 11: ... similar to Fig. 10 but for the $n \to \pi^- p$ process ...

Figure 12: ... angular dependence ...

Description of Fig. 11.
Description of Fig. 12 for angular dependence.

1.2 Fracture Functions, or Conditional Structure Functions

Deep–inelastic electron–nucleon scattering (DIS) has been one of the principal sources of information about the dynamics of strong interactions at distances $\ll 1\,\mathrm{fm}$ and the internal structure of the nucleon. In the simplest case such experiments measure the *inclusive* cross section $eN \to e'X$ in the region of large energies and momentum trasfers, $W^2, Q^2 \gg 1\,\mathrm{GeV}^2$. Thanks to the asymptotic freedom of QCD this cross section can be factorized into the cross section for scattering from a quasi–free parton (quark, antiquark), which takes place over distances $\sim 1/Q$ and is calculable using perturbation theory, and the so-called parton density, which describes the light–cone momentum distribution of the quarks and antiquarks in the nucleon, as arising from non-perturbative dynamics at distances $\sim 1\,\mathrm{fm}$ (see Fig. 13a,b). The parton densities are rigorously defined as nucleon matrix elements of certain QCD composite operators and can be calculated using non-perturbative methods such as Lattice QCD. QCD radiation (bremsstrahlung with momenta ranging up to $\sim Q$) leads to an effective logarithmic dependence of the parton densities on Q^2, described in a simple way through evolution equations (DGLAP).

An important consequence of factorization is that the parton densities do not depend on the specific scattering process used to measure them; e.g., the same densities appear also in neutrino-induced DIS, Drell-Yan pair production in pp collisions, jet production, etc. This *"universality"* ensures that the parton densities are objective measures of nucleon structure in QCD. Considerable efforts have been devoted to extracting the parton densities from fits to data from various high-energy scattering processes. The results of these fits have provided many interesting insights into nucleon structure, such as the presence of a non-perturbative flavor-asymmetric "sea" of antiquarks at the hadronic scale [20, 21]; a large non-perturbative density of gluons [22, 23, 24], and the distribution of the

nucleon spin over its quark and gluon constituents [25, 26]. Experiments with the JLab 12 GeV Upgrade will provide crucial new information about the parton densities at large light-cone momentum fractions $x \to 1$ and the spin distribtutions [27].

Much more information about nucleon structure and QCD dynamics can be gained from measurements of DIS with *identified hadrons* in the final state, $eN \to e' + h + X'$. The final state in DIS measurement is generally divided into three regions: (a) the current fragmentation region, containing hadrons produced by fragmentation of the struck quark; (b) the target fragmentation region, containing hadrons produced in the breakup of the target nucleon; (c) a central region, populated by hadrons produced through QCD radiation and/or hadronization of small–x partons. The precise identification of these regions depends on the variables used to characterize the final state (rapidity, energy fraction z, Feynman variable x_F), and different conventions are used in the literature. In DIS experiments at JLab with 11 GeV energy it is generally expected that a reasonable separation of current and target fragmentation regions can be achieved using the standard criteria (e.g. $x_F < 0$ and > 0); a central region is absent because of the limited energy. An extensive program of DIS experiments in the current fragmentation region (semi-inclusive DIS) is planned with 11 GeV, with the aim to measure the flavor structure of the nucleon and certain transverse momentum–dependent distributions of quarks (TMDs).

Equally — and in some respects even more — interesting is the study of hadron production in the target fragmentation of DIS, $eN \to e' + h$(target region)$ + X'$, which represents a particluar conditional case of inclusive DIS. QCD factorization for the single–hadron inclusive cross section in this region was proved in Refs. [37, 29] and proceeds along the same lines as for fully inclusive scattering, with the hard parton–level process the same as in the inclusive case (see Fig. 13c). Bjorken scaling of the cross section for a fixed hadron momentum $|\mathbf{p}_h| \ll Q$ (in the target rest frame) is expected to occur on the same grounds as in inclusive scattering and serves as a powerful test of the production mechanism. The partonic structure of the target is now described by a *conditional parton distribution* (or fracture function) which depends not only on the light–cone momentum fraction of the parton, x, but also on the momentum of the produced hadron in the target fragmentation region, usually described by the variables

$$\beta \;\equiv\; \frac{p_h^+}{(1-x)P^+} \quad \text{Light-cone momentum fraction of observed hadron}$$
$$p_{Th} \;\equiv\; |\mathbf{p}_{Th}| \quad \text{Transverse momentum of observed hadron} \tag{10}$$

Alternatively, one uses the invariant momentum transfer between the target nucleon and the produced hadron, defined as

$$t \;\equiv\; (p_h - p_N)^2 \tag{11}$$

The conditional parton distribution $f_q(x, \beta, t)$ describes the probability to find a hadron h with light-cone momentum β_h and p_{Th} in the nucleon *after removing* a quark of type q with light-cone momentum fraction x (see Fig. 13d). Just as the usual parton densities, they are independent of the hard scattering process that removed the parton and represent the objective structure of the target. The conditional parton densities at fixed hadron

Figure 13: Factorization in deep–inelastic scattering. (a) Inclusive DIS $eN \to e' + X$. The scattering process takes place on a quark in the target (b) Parton distribution $f(x)$. It describes the probability distribution of quarks with respect to their light-cone momentum fraction x in the target (c) Conditional cross section with an identified hadron in the target fragmentation region $eN \to e' + h(\text{target}) + X$. Factorization is performed in analogy to the inclusive case. (d) Conditional parton distribution. It describes the probability to find a hadron h in the target fragmentation region, with light-cone momentum fraction β and transverse momentum $\mathbf{p}_T$, after removing a quark with light-cone momentum fraction x.

momentum obey the *same* QCD evolution equations as the usual PDFs,[1] allowing one to compute their scale dependence from first principles and compare results of experiments at different Q^2.

The conditional PDFs contain a wealth of interesting information about nucleon structure and non-perturbative dynamics. Different physical interpretations are being considered in different regions of the parton momentum fractions x:

- At $x \ll 1$ the conditional PDFs for nucleon production in the target fragmentation region ($h = p, n$) describe the partonic content of the "meson–like" system exchanged between the target nucleon and the operator measuring the parton density (t–channel picture). Depending on the energy region and the quantum numbers this can be a Regge trajectory, a single meson, or a multi–meson state. Particularly interesting examples are

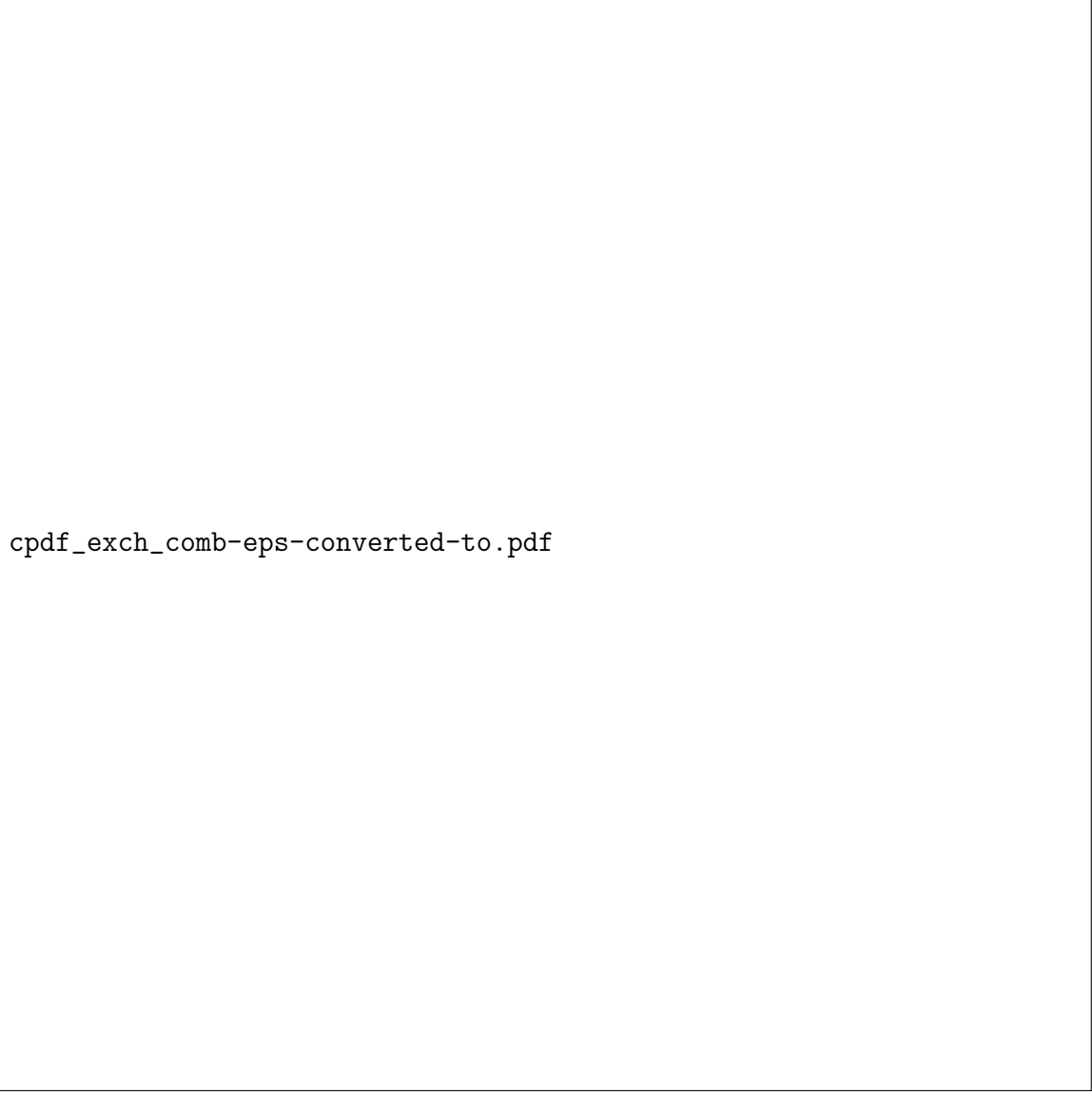$$p \rightarrow p, \qquad x \ll 0.1 \qquad \text{Pomeron exchange} \tag{12}$$

$$p \rightarrow n \ \text{ or } \ n \rightarrow p, \qquad x \sim 0.1 \qquad \text{Charged pion exchange} \tag{13}$$

  The conditional PDF in these regions is given by the product of the light-cone momentum distribution of the exchanged system ("flux") and the parton density of the exchanged system. The channel Eq. (12) was explored at HERA and gave rise to a very successful description of conditional PDFs in terms of the partonic content of the pomeron [31, 32, 33]. The channel Eq. (12) represents a unique method for measuring the parton distributions of the pion and will be explored in the present experiment (see below) [31]. The pionic contribution to the conditional PDF can be rigorously identified by extrapolating in the variable t to the pole at $t = M_\pi^2$ (unphysical region).

- In the region $x > 0.3$ the DIS process on the nucleon predominantly "knocks out" a valence quark, leaving behind a system with a "hole" in the color/spin/flavor wave function. Production of hadrons in the target fragmentation region reveals how such a system with a hole materializes in physical hadrons. This represents a fundamental process of QCD and provides important information about non-perturbative dynamics, such as the role of dynamical chiral symmetry breaking (constituent quarks as effective degrees of freedom, short-range non-perturbative forces) and color confinement in hadron formation. It is also provides new insight into nucleon structure, as the hadronization process is sensitive to the isospin (flavor structure) and spin of the initial nucleon and produced hadron system. Target fragmentation in this region of x is largely unexplored and remains a major potential source of information on nucleon struture.

---

[1]Some authors consider the conditional parton densities integrated over the hadron transverse momenta (fracture functions) [37]. Their QCD evolution equation differs from the standard DGLAP equations by an inhomogeneous term, which describes the feed-down of hadrons produced by fragmentation of partons appearing through QCD radiation [37]. Here we consider the conditional parton densities at fixed momenta $p_{Th} \ll Q$, for which this effect is parametrically suppressed, and which obey the usual DGLAP evolution equations [29].

Figure 14: (a) Conditional PDF for production of a nucleon (proton) in the target fragmentation region. (b) Interpretation in terms of t–channel exchange at $x \ll 0.1$. (c) Interpretation as materialization of nucleon remnant with hole in the valence–quark dominated region $x > 0.3$.

Here we propose a pioneering measurement of conditional DIS with nucleon production in the target fragmentation region using the JLab 11 GeV electron beam, the Hall A Super BigBite spectrometer for electron detection, and a dedicated time projection chamber for recoil proton tagging. The conditional cross section for proton production will for the first time be measured both for a proton *and a neutron target*, $e+p$ (or n) $\rightarrow e'+p+X$; the latter channel will be identified using an innovative method of scattering from a deuterium target and tagging two low-momentum recoil protons at backward angles, $eD \rightarrow e' + p + p + X$. The objectives of this experiment are:

I) Establish the QCD-based reaction mechanism for nucleon production in the target fragmentation region at JLab energies by testing model-independent features such as Bjorken scaling at fixed recoil momentum (β, t), and investigating the kinematic dependences;

II) Measure the conditional PDFs for both $p \rightarrow p$ and $p \rightarrow n$ transitions, particularly their isospin depdendence, compare it with dynamical models and measurements at higher energies (COMPASS, HERA) using DGLAP evolution;

III) Extract the pion exchange contribution to the conditional PDFs and relate it to the parton desity of the pion, as measured also in other reactions (Drell-Yan pair production in πA scattering), testing its universality and providing new information about its strength at large values of z (quark/antiquark momentum fraction in pion).

Measurements of proton and neutron production in the target region have been performed at the HERA collider at $x < 10^{-2}$. Target fragmentation into baryons, especially Λ hyperons (whose spin polarization can be detected through their decay), is also measured at the CERN COMPASS experiment [30]. Nucleon production in the valence region $x > 0.1$ remains unexplored and would for the first time be measured in the JLab12 experiment. The proposed experiment is thus complementary to the existing measuerements and would substantially broaden our knowledge of target fragmentation. The projected results can be related to the high-energy measurements through DGLAP evolution, testing the universality of the conditional PDFs. It is important to note that the data from high-energy experiments such as COMPASS are at *both higher Q^2 and smaller x* — exactly the region connected to the JLab region by the evolution flow. In particular, the measurement of the isospin dependence (p–n difference) of the conditional PDFs would settle the question of the relative importance of singlet and non-singlet exchanges in target fragmentation, which cannon be answered from the high–energy data alone.

Measurements of the $n \rightarrow p$ conditional PDF represent a clean (parametrically contolled) method for probing the partonic content of the nucleon's pion cloud in inclusive scattering and extracting information about the pion PDF. Taking advantage of the additional kinematic variable t, the pionic contribution to the conditional PDF can be rigorously defined as the residue of the pole at $t = M_\pi^2$, which can be extracted from the data by extrapolating to the unphysical region. The physical region of t in conditional DIS with a nucleon in the target fragmentation region is

$$-t \;>\; -t_{\min} \;\equiv\; \frac{y^2 M_N^2}{1 - y}, \qquad y > x, \tag{14}$$

where y is the pion light-cone momentum fraction in the nucleon, $1 - y = \beta(1 - x)$. In DIS measurements at JLab energy the kinematically accessible values of t are rather large, $-t > 0.1\,\mathrm{GeV}^2$ for $x \sim 0.3$, so that one cannot rely on dominance of the pion pole alone but has to use dynamical models to separate pole and non-pole (background) contributions. Even so, measurements of the conditional PDFs can constrain the parton densities of the pion and provide interesting information about non-perturbative dynamics.

In the kinematic range accessible with JLab at 11 GeV the interpretation of hadron production in the target fragmentation region is in several ways simpler than that of semi-inclusive DIS in the current fragmentation region, which is widely discussed as a possible way to probe the transverse momentum–dependent (TMD) quark distributions in the nucleon [27]. In current fragmentation one aims to extract the transverse momentum distribution of *partons* relative to the target hadron, which can be inferred only indirectly through the hadronic jet (broadening by the transverse momentum of the hadronization process) and is affected in a complex manner by QCD radiation (Sudakov–suppressed evolution). In contrast, target fragmentation we measure the longitudinal and transverse momentum of an identified *hadron* relative to the target hadron, which is directly observable and can be interpreted in terms of nucleon structure; e.g., it provides the invariant t which allows one to isolate definite exchange mechanisms. The QCD evolution of the conditional PDFs is the standard DGLAP evolution, which has been tested extensively in inclusive DIS and shown to work reliably down to the scales $Q^2 \sim$ few GeV^2 accessible at JLab. Finally, since at JLab energies the current and target fragmentation regions are not widely separated, a quantitiative understanding of target fragmentation (longitudinal and transverse momentum distribution of target hadrons) will be a prerequisite also for the analysis of semi-inclusive DIS in the current fragmentation region.

1.3 Measurement of the Pion Structure Function via the Sullivan Process

The pion, being the lightest and simplest hadron, has a central role in our current description of nucleon and nuclear structure. The pion has been used to explain the long-range nucleon-nucleon interaction and also to explain the flavor asymmetry of the quark sea in the nucleon. Moreover, the masses of light mesons such as the pion are believed to arise from dynamical chiral symmetry breaking [40], and thus models of the pion must account for both its role as the Goldstone boson of quantum chromodynamics (QCD) and as a quark-antiquark system.

Experimental knowledge of the partonic structure of the pion is very limited due to the lack of a stable pion target. Most of the current knowledge of the pion structure function in the valence region is obtained primarily from pionic Drell-Yan scattering [41]-[43], and in the pion sea region at low Bjorken-x, from hard diffractive processes measured on $e - p$ collisions at HERA [44]. The existing data on the pion structure function from Drell-Yan scattering is shown in Fig 15. Also shown, in Fig. 16, are the pion structure function at low x deduced from hard diffractive process, where forward-going neutrons or protons were tagged in coincidence with the DIS events. These results seem to indicate that the pion sea has approximately one-third of the magnitude of the proton sea, while from the parton model one expects the pion sea to be two-thirds of the proton sea.
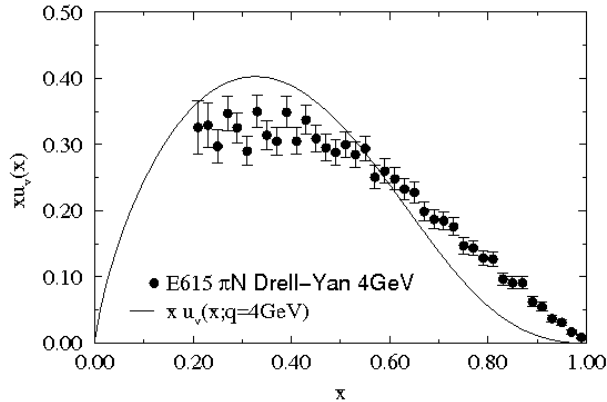
Figure 15: Existing data for the pion structure function from Drell-Yan Experiment E615 [41]. The solid curve is the calculation from Ref. [48].

There are several theoretical calculations of the pion structure in the valence region, however, they tend to disagree with each other. The parton model [45], perturbative QCD based models [46, 47] and some non-perturbative models such as those based on the Dyson-Schwinger Equation [48]-[51] predict a $(1-x)^a$ dependence with $a \geq 2$. On the other hand relativistic constituent quark models [52, 53], Nambu-Jona-Lasinio models [54]-[57], the Drell-Yan-West relation [58, 59] and even arguments based on quark-hadron duality [60] favor a linear $(1-x)$ dependence of the pion structure function at high-x. Calculations of the pion structure function in the pion sea region, such as those of the chiral quark model [61], also disagree with the extraction from the HERA data, in fact these models predict that the momentum fraction of pion sea is larger than the proton sea. These discrepancies tell us that it is essential to measure the pion structure function over a wide range of x using new techniques.

One such technique is to measure the contribution to the electron Deep Inelastic Scattering (DIS) off the meson cloud of a proton target, as pointed out by Sullivan[62] (Fig. 17). This so-called Sullivan process was shown to persist even at large Q^2 scales. An immediate consequence of the Sullivan process is that the nucleon parton distributions contain a component which can be attributed to the meson cloud. This intriguing idea remained untested for many years. In the early 1980s, Thomas [63] predicted several implications of the Sullivan process for nucleon parton distributions using a cloudy-bag model for describing the meson cloud. In particular, it was predicted that the nucleon sea should have an up/down sea-quark flavor asymmetry, as well as an s/s̄ asymmetry for the strange quark sea. The earliest parton models assumed that the proton sea was flavor symmetric, even though the valence quark distributions are clearly flavor asymmetric. The assumption of flavor symmetry was not based on any known physics, and it remained to be tested by experiments. A direct method to check this assumption is to compare the sea in the neutron to that in the proton by measuring the Gottfried integral in DIS. The Gottfried Sum Rule (GSR) gives the following relation for the proton and neutron structure functions F_2^p and F_2^n:

$$I_{\text{GSR}} = \int_0^1 [F_2^p(x) - F_2^n(x)]/x dx = \frac{1}{3} + \frac{2}{3} \int_0^1 [\bar{u}(x) - \bar{d}(x)] dx = \frac{1}{3}. \qquad (15)$$
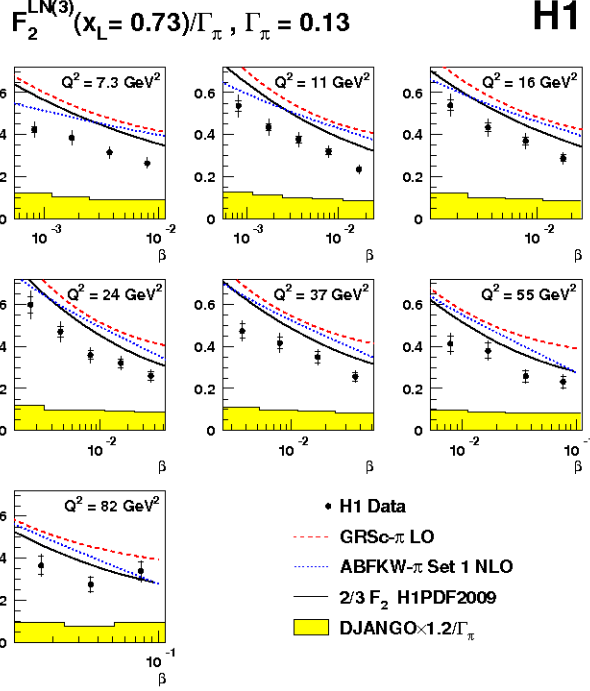
21

Figure 16: Pion structure functions measured by H1 [44] in comparison with parameterizations of various pion parton distribution functions. The Bjorken-x of the pion is denoted as β.

In the early 1990s, the NMC collaboration reported[64] an observation of the violation of the GSR[65], $I_{\rm GSR} = 0.235 \pm 0.026$. Since the GSR is derived under the assumption of $\bar{d}(x) = \bar{u}(x)$, the NMC result strongly suggests that this assumption is invalid. Indeed, Eq.1 and the NMC result imply that

$$\int_0^1 (\bar{d}(x) - \bar{u}(x))dx = 0.148 \pm 0.039 \tag{16}$$

Independent confirmation of the $\bar{d}/\bar{u}$ flavor asymmetry were later provided by Drell-Yan experiments [66, 67, 68, 69] and the semi-inclusive DIS experiment [70]. Figure 18 shows the E866 result on $\bar{d}(x) - \bar{u}(x)$ at $Q^2 = 54$ GeV$^2/c^2$. The surprisingly large asymmetry between $\bar{d}$ and $\bar{u}$ is observed over a broad range of x. The E866 data provide a direct evaluation of the $d - u$ integral, namely, $\int_0^1 (\bar{d}(x)\bar{u}(x))dx = 0.118 \pm 0.012$, which is in good agreement with the NMC result shown in Eq. 2. The observation of $\bar{u}, \bar{d}$ flavor asymmetry has inspired many theoretical work regarding the origin of this asymmetry. Perturbative QCD, in which $q\bar{q}$ sea is generated from the $g \to q\bar{q}$ splitting, has difficulties explaining such an asymmetry. The small d, u mass difference (actually, $m_d > m_u$) of 2 to 4 MeV compared to the nucleon confinement scale of 200 MeV does not permit any appreciable difference in their relative production by gluons.

At any rate, one observes a surplus of $\bar{d}$ which is the heavier of the two species. Field and Feynman long time ago speculated that the $g \to u\bar{u}$ process would be suppressed relative to $g \to d\bar{d}$ due to Pauli-blocking effect and the presence of two u-quarks as compared
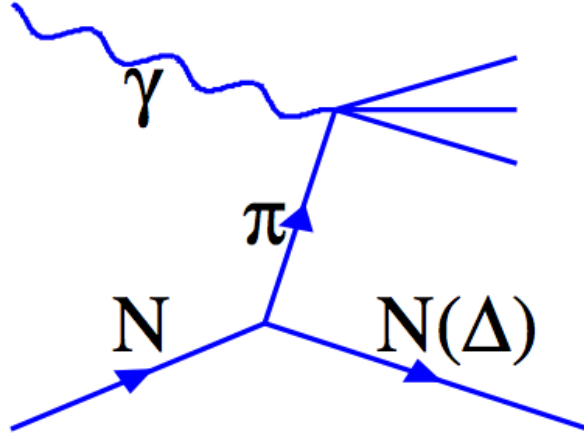
Figure 17: The Sullivan process

to a single d-quark in proton. Steffen and Thomas have examined the consequences of Pauli-blocking, concluding that the effect of blocking is small [71]. Thus, another, presumably non-perturbative, mechanism must account for the large measured $\bar{d}$, $\bar{u}$ asymmetry. Many of the non-perturbative approaches to explain the $\bar{d}$, $\bar{u}$ asymmetry involve the use of isovector meson (particularly pion). Recent reviews [72, 73, 74] have extensive discussions on various theoretical models. In the meson-cloud model, the virtual pion is emitted by the proton and the intermediate state is pion + baryon. More specifically, the proton is taken to be a linear combination of a "bare" proton plus pion-nucleon and pion-delta states, as below,

$$|p> \quad \rightarrow \quad \sqrt{1-a-b}|p_0> +\sqrt{a}(-\sqrt{\frac{1}{3}}|p_0\pi^0> +\sqrt{\frac{2}{3}}|n_0\pi^+>)$$

$$+\sqrt{b}(\sqrt{\frac{1}{2}}|\Delta_0^+\pi^-> -\sqrt{\frac{1}{3}}|\Delta_0^+\pi^0> +\sqrt{\frac{1}{6}}|\Delta_0^0\pi^+>) \qquad (17)$$

The subscript zeros on the virtual baryon states indicate that they are assumed to have symmetric seas, so the asymmetry in the antiquarks must be generated from the pion valence distribution. The coefficients a and b are the fractions of the πN and $\pi \Delta$ configurations, respectively, in the proton. These fractions can be calculated using the πNN and $\pi N\Delta$ couplings, and form factors as taken from experiment. The asymmetry in the proton sea arises because of the dominance of π^+ among the virtual configurations. Figure 18 shows that the pion-cloud model can reproduce the x-dependence of the $\bar{d}\bar{u}$ distribution very well. The success of the meson-cloud model in explaining the $\bar{d}$, $\bar{u}$ asymmetry suggests that a direct measurement of the meson cloud in DIS should be feasible. The idea is that the meson cloud in the nucleon could be considered as a virtual target to be probed by various hard processes including DIS and Drell-Yan.

In summation,

- the partonic structure of the pion, the lightest and simplest hadron is not well
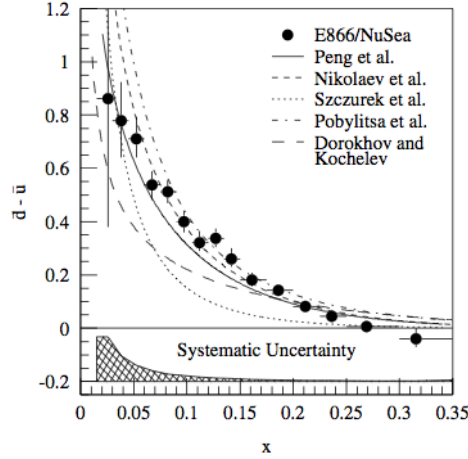
Figure 18: Comparison of the E866 $\bar{d}\bar{u}$ data with various model calculations [69]

measured over the entire Bjorken-x range and the predictions of models describing the pion structure differ significantly. There is a great need to measure the pion structure with a new and independent technique.

- The well established quark flavor asymmetry in the nucleon sea can be explained in terms of the meson cloud model.

- The Sullivan process allows access to the meson cloud of the nucleon. Measurements at JLab would allow a rigorous determination of the pion-cloud content of the nucleon, and test the theoretical models that explain the dbar/ubar asymmetry, observed in the Drell-Yan experiments, in terms of the pion cloud.

- Using the Sullivan process to measure the pion structure function would help establish the mesonic content of the nucleon and also provide a new and independent method to access the partonic structure of the pion.

- The measurement of pion parton distribution using the Drell-Yan process (Fermilab E615 and possibly at COMPASS in the future) is limited to charged pions. At JLab, the measurements can be extended to neutral pion and check the validity of isospin symmetry.

The idea of considering the meson cloud as a virtual pion target was used at the HERA $e - p$ collider to measure the pion structure functions at low-x in a hard diffractive process, where forward-going neutrons or protons were tagged in coincidence with the DIS events, as shown in Fig. **??**. While the HERA experiments have provided very interesting first data on the extraction of pion structure functions using the Sullivan process, there are many reasons for extending such measurements to JLab energies. First, the HERA kinematics is limited to very low x region, where no independent measurement of pion structure functions exists. This makes it difficult to check the validity of the interpretation of the HERA data in terms of the meson-cloud model. The 12 GeV upgrade of JLab will allow access kinematics of $|t| < 0.2$ GeV^2, $Q^2 > 1$ GeV^2 and $M_x > 1.0$ GeV/c^2, which

24

will enable us to probe the high and intermediate x region of the pion, where some data on the structure functions already exist from the pion-induced Drell-Yan experiments. A comparison of the x-dependence of the pion structure function deduced from the Sullivan process and the Drell-Yan process would provide a very stringent test of the pion-cloud model. Second, the large angular and kinematic coverage for the re-coiling proton (or proton pair) detected using the BONUS-12 recoil detector, in coincidence with the scattered electron, would allow a detailed study of the Sullivan process as a function of several variables including the recoiling proton momentum and angles. Third, the electron will be detected in the SBS with the hadron calorimeter replaced with the large angle calorimeter (LAC), or in the BigBite spectrometer. The SBS and recoil detector may allow a detection of the $\Lambda \to p\pi^-$ decay, making a measurement of the $p \to K^+\Lambda$ kaon cloud in the nucleon potentially feasible. This could lead to a measurement of kaon structure functions. Finally, the Sullivan process could contribute to the proposed $d(e, e'p)X$ measurement of the neutron structure function (BONUS-12). It is important to determine experimentally the magnitude of the Sullivan process by detecting both the $p(e, e'p)X$ and $d(e, e'pp)X$ reactions. Such measurements would provide crucial inputs needed for an accurate extraction of the neutron structure functions. The charged pion exchange process has the advantage of less background from Pomeron and Reggeon process [75] and the charged pion cloud is double of the neutral pion cloud in the proton.

In this experiment we will measure the semi-inclusive structure function of the leading proton, $F_2^{LP(4)}$, which is related to the measured cross-section as;

$$\frac{d^4\sigma(ep \to e'Xp')}{dxdQ^2dydt} = \frac{4\pi\alpha^2}{xQ^4}(1 - y + \frac{y^2}{2[1+R]})F_2^{LP(4)}(x, Q^2, y, t), \tag{18}$$

where $y = P.q/P.l$, $Q^2 = -(l - l')^2$, $x = Q^2/(2P.q)$ and $t = (P - P')$ where $P(P')$ are the initial(scattered) proton 4 vector, $q = l - l'$ and $l(l')$ are the initial (scattered) lepton and R is the ratio of the cross-section for longitudinally and transversely polarized virtual photons. The measured cross-section can be integrated over the proton momentum (which is effectively an integration over t [44]) to obtain the leading proton structure function $F_2^{LP(3)}$. The pion structure function F_2^π can then be extracted from $F_2^{LP(3)}$ using models, such as the Regge model of baryon production. In the Regge model the contribution of a specific exchange i is defined by the product of its flux $f_i(y, t)$ and its structure function F_2^i evaluated at (x_i, Q^2). Thus,

$$F_2^{LP(3)} = \sum_i [\int_{t_0}^{t_{min}} f_i(z, t)]F_2^i(x_i, Q^2), \tag{19}$$

where i is pion ρ-meson etc, and the t corresponds to the range of p_T analyzed.

The extraction of the pion structure function will have to be corrected for a number of complications to this simple picture, such as the absorptive effect of other mesons. However, these corrections are minimized by measuring at the lowest proton momentum possible from the reaction. This minimizes the absorptive correction since at lower momenta the pion cloud is further from the bare nucleon. In addition, the low proton momentum ensures that the higher meson mass exchanges are suppressed by the energy denominator. These and other corrections are discussed below.
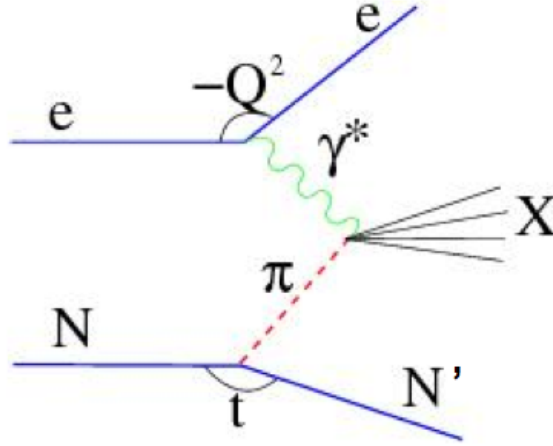
Figure 19: Kinematics diagram for electron scattering from the pion cloud of the nucleon N. The initial nucleon is at rest.

The largest uncertainty in extracting the pion structure function arises from the knowledge of the pion flux in the framework of the pion cloud model. One of the main issues is whether to use the πNN form factor or the Reggeized form factor. The difference between these two methods can be as much as 20% [77]. From the N-N data the πNN coupling constant is known to 5% [78]. If we assume that all corrections can be performed with a 50% uncertainty and we assume a 20% uncertainty in the pion flux factor, the overall systematic uncertainty will be 24%. However, by comparing to pionic Drell-Yan data at moderate x (where it is most reliable), we can have a measurement of the pion flux factor. For example the pion structure function at x=0.5 has been measured from the pionic Drell-Yan data to an accuracy of 5% [?].

2 Experiment

2.1 Overview

We propose to measure the semi-inclusive reactions $p(e, e'p)X$ and $D(e, e'pp)X$ for $Q^2 >0.5$ $(\text{GeV/c})^2$ at very low proton momenta $(60 - 400)$ MeV/c. The key to this experimental technique is to measure the low-energy outgoing target proton in coincidence with a deeply inelastically scattered electron, as shown in Fig.19. The inclusive electron kinematics determine that a DIS event has occurred, i.e. that the reconstructed Q^2 and W^2 are large. However, unlike the standard inclusive case, the low momentum protons measured in time and vertex coincidence with the DIS event ensure that the deep inelastic scattering occured from partons within the meson cloud surrounding the nucleon. This can be achieved by employing the Super BigBite Spectrometer to detect the scattered electrons in time and vertex coincidence with low momentum proton(s) measured in a low mass radial time projection chamber (RTPC, a BONUS-like detector).

2.2 Luminosity

The subject of the proposed experiment is an essential feature of the proton internal structure, specifically, a quark-quark correlation related to the meson cloud associated with a (fluctuating/recoiling) nucleon. In spite of enormous developments in the field of nucleon structure over the last 65 plus years since the original Fermi and Marshall 20% number was given for the pion-nucleon component of the nucleon wave function, this estimate endures without signifiant change. However, the experimental signature of the pion in the nucleon remains under debate.

A fixed-target experiment at kinematics with modest momentum transfers and higher x_{Bj} will compliment the already performed HERA experiments which investigated diffractive DIS in a collider regime with a 800 GeV proton beam on a 30 GeV positron beam. The proposed study of TDIS through detection of a very low energy proton in coincidence with a scattered electron DIS event will measure a very different part of the reaction space, one that can be rigorously evolved to the HERA kinematics, as well as related to the long-searched-for Sulivan process.

In this section we present a set of considerations concerning the Figure-of-Merit for this experiment, a product of electron-nucleon luminosity ($\mathcal{L}$), electron detector acceptance (Ω_e), and recoil proton detection efficiency (η_p), required for TDIS investigation. The level of luminosity which may be used in the proposed experimental setup is also constrained by the signal size and, critically, the experimental background rates.

The cross section of the inclusive DIS process for an 11 GeV electron beam scattered from a proton target is very well known, see e.g. the PDG report [?]. A traditional measurement of the DIS cross section with 1% precision with minimum DIS requirements on Q^2 and W^2 does not require much time with any electron spectrometer at Jefferson Lab, and experiments have been approved that will do this, extending the existing body of data in this kinematic regime from SLAC and other laboratories. The (unmeasured) percentage in total of such events coming from the meson cloud of the proton target should be approximately 20%. However, the fraction of DIS events in coincidence with a *low energy* proton is much smaller than the total meson-nucleon part of the wave function. According to recent calculations, as above, the fraction of DIS events with proton momenta below 250 MeV/c and the direction in the detector acceptance (above 30° with the beam direction), $F_{\pi p}(x_{Bj}, \Delta k)$, is about 0.1% [?].

Such a small fraction leads to a low rate of true coincidence events between the DIS-scattered electron and the recoiling, target proton. Therefore, the proposed experiment requires a large FOM and good control of accidental coincidences. The accidental coincidence events are mainly due to a large rate of low energy protons produced in low momentum transfer reactions, such as small angle electron elastic scattering and pion photoproduction. In the deuteron, one needs to also consider photodisintergration into proton-neutron pairs.

In spite of a very high total rate of the low energy protons in elastic electron-proton scattering (at the momentum $p_p > 70$ MeV/c and luminosity 3×10^{36} cm^{-2}/s the rate is about 200 MHz), the rate in the angular range $\theta_p < 70°$ is relatively small (200 kHz). Another source of low energy protons is a photoproduction mechanism which was found to be 3 MHz at the proposed luminosity of 3×10^{36} cm^{-2}/s and in the momentum and

angular range of interest. For details, see the discussion in this proposal of abckground simulation.

There are three parameters which allow rejection of the accidental protons:

- The polar angle between the proton track and the beam direction.

- The correlation in time between an electron hit and a proton hit.

- The correlation between the vertices of electron and proton tracks.

The projected polar angle resolution of the RTPC of 1◦ will allow rejection of the range of angles where most elastically recoiled protons are located. The projected time resolution of the RTPC of 10 ns allows for a narrow 20 ns timing cut in offline data analysis. A significant length of the RTPC target cell (40 cm), combined with the good vertex resolution of the SBS spectrometer, will provide additional suppression of accidental events by a factor of 10. The resulting accidental probability is expected, then, to be 0.003.

The projected level of the signal to accidental rate varies with x_{Bj}, see Tab. 1. For illustration purposes, in Fig. 20, we show the event distribution over $dz = z_p - z_e$ after other cuts are applied for two levels of the signal to the background ratio 1/10.
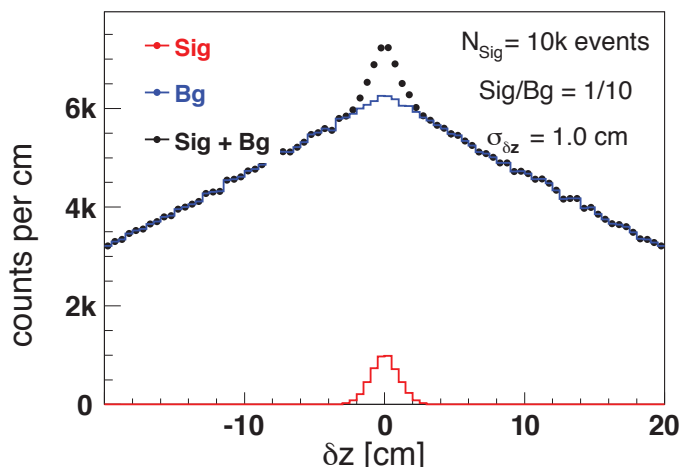

Figure 20: The projected event distribution over $\delta z = z_p - z_e$ for the ratio of signal to background of 1/10.

For the maximum beam energy available in Hall A, 11 GeV, and DIS requirements ($W^2 > 4$ GeV^2, $Q^2 > 1$GeV^2), a total cross section in the range of $x_{Bj} \approx 0.1$ is of the order of 1×10^{-32} cm^2/sr/dx_{Bj}. For the Super Bigbite spectrometer as an electron arm at the central angle of 12° the solid angle is about 50 msr.

The pilot experiment presented in this proposal will use a 40-cm long Radial Time Projection Chamber, RTPC, and a Super Bigbite spectrometer at 12° in-plane central scattering angle (with total solid angle of 50 msr). The projected statistics for several x_{Bj} bins (all collected at the same time) are presented in Tab. 1.

For the measurement at higher x_{Bj} up to 0.15 where expected value of e-p events is smaller (see Fig. 21) we plan to reduce the luminosity to 1×10^{36} cm^{-2}/s and collect data

x_{Bj} (in ± 0.01 range)	0.07	0.09	0.11	0.13	0.15
H(e,e') events	23.4M	23.4M	23.4M	23.4M	23.4M
true coincidence events	61k	33k	19k	9k	3k
accidental events	42k	42k	42k	42k	42k
signal to background ratio	1.44	0.78	0.45	0.21	0.07
resulting $\delta S/S$ stat. accuracy [%]	0.53	0.83	1.3	2.5	7.1

Table 1: Projected statistics of TDIS events for the proton momentum range 60-250 MeV/c (corrected for the efficiency factors of SBS (0.9) and RTPC (0.6)) for several x_{Bj} bins from the first part of the proposed data taking run (10 days). The dash cyan line shows the level of fracture functions which could be measured with 7% statistical accuracy in ten-day run at luminosity 3×10^{36} cm^{-2}/s.

for an additional period of 10 days. It is at these kinematics that the projected drop in the meson cloud distribution, and consequently in the fracture function, should be most apparent.
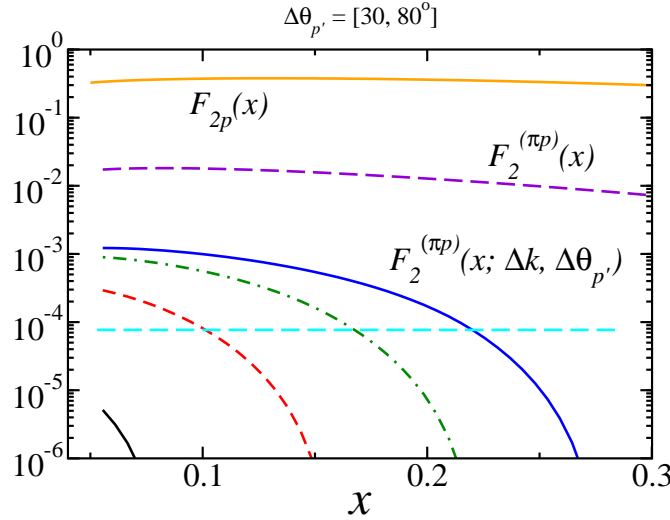

Figure 21: The proton SF F_2^p, the pion related part $F_2^{(\pi p)}$, and the fraction $F_2^{(\pi p)}(\Delta k, \Delta \Theta_h)$ vs x_{Bj} for the proton momentum intervals, Δk: in MeV/c - black (60-100), red (100-200), green (200-300), blue (300-400) and the cut on the angle between the proton and the virtual photon momentum directions, Θ_h, between 30° and 80°.

2.3 Recoil Detector

Detection of a soft nucleon is complicated by a large intensity of the secondary electrons, photons, and soft nucleons produced in the interaction of the high energy electron beam with the target. A proton detection option has several essential advantages over neutron detection, as were leveraged by the BONUS and CLAS eg6 experiments:

- The ionization density in the soft proton track for the momentum range 60-250 MeV/c is very high, which allows effective suppression of the secondary electron and soft photon induced signals.

- The protons of interest (2.5 - 20 MeV kinetic energy) have momenta perpendicular to the beam direction much larger than typical perpendicular momentum of the secondary electrons which allows us to use magnetic separation of the proton and electron background using a solenoidal magnet.

- The proton track allows for reconstruction of the event vertex and direction, which are powerful means for rejection of accidental events.

- The proton detector readout segmentation could be on the level of 10^5 or above, which is at least a factor of 100 times higher than practical for a neutron detector.

The recoil detector will be fundamentally the same as the cylindrical RTPC being developed for the experiment to measure the structure function of the free neutron (E12-06-103, or BONUS-12), the latter being based on the very successful cylindrical RTPCs that were employed for the BONUS and CLAS eg6 experiments as pictured in Fig. 22. The proposed RTPC will, however, utilize a different solenoid. This is an existing solenoid, shown in Fig. 23, with a 400-mm warm bore, a total length of 152.7 cm, and a superconducting coil that operates with a 47 kG magnetic field in the center of the magnet. Simulation studies have shown that increasing the radial drift region by a factor of 2 compared to the BONUS and eg6 RTPC detectors can provide a 50% relative improvement in the momentum resolution, as well as extend the momentum range of the detector. This magnet and RTPC will have a larger radial drift distance than that proposed for BONUS-12. The enhanced drift region will facilitate measurements of proton momenta up to 400 MeV/c or more with a resolution of 3%. The length of this magnet is also a help, allowing us to use a longer (40 cm) target for improved background rejection and luminosity.

The proposed TDIS RTPC will be 40 cm long and consist of an annulus with inner radius of 5 cm and an outer radius of 15 cm. The amplification of the drifting electrons will be achieved by three layers of cylindrical Gas Electron Multiplier (GEM, see Ref. [83]) foils at radii of 15 cm. This will be surrounded by a cylindrical readout surface featuring elongated pads. GEMs are 50 μm thick polyamide foils coated on both sides with a 5 μm copper layer and punctured with 70 μm holes. The distance between these holes is about 140 μm. By applying a voltage in the range of 200 V to 300 V across the two copper layers a very high electric yield is formed inside the holes. Electrons drifting towards the GEM foil produce an avalanche of secondary electrons when captured and accelerated through the holes. The total gain in GEM will be of the order of 100. The electrons are transferred to the next GEM foil and after passing three GEM foils the resulting electron pulse is detected on the readout plane. The full length of the RPTC could be be closer to 60 cm to accommodate protons emitted at angle as small as 30° relative to the beam direction.

As with BONUS and CLAS eg6, materials between the target and the sensitive detector volume have to be minimized to prevent energy loss of the protons and to minimize
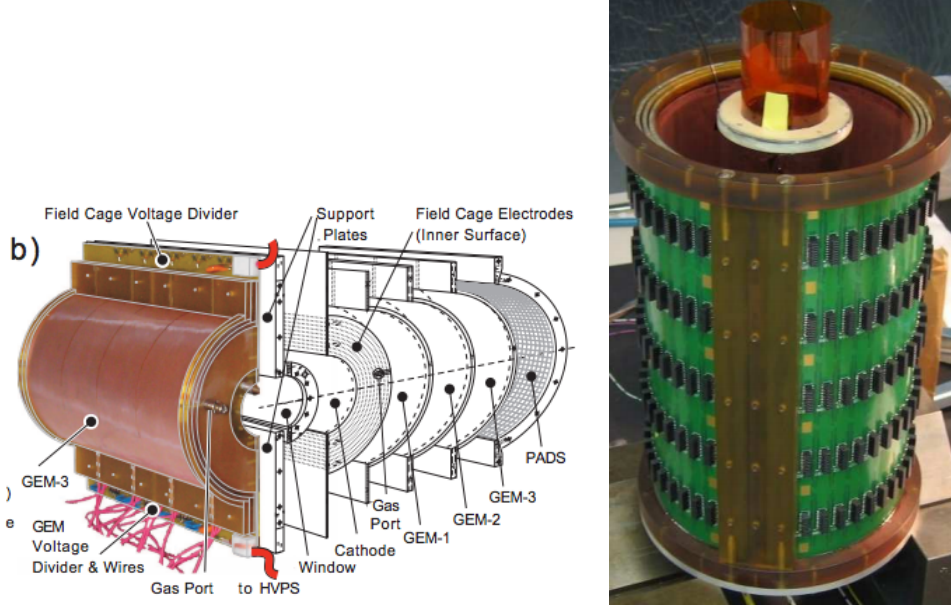
Figure 22: (left) Photograph of the BoNuS RTPC, showing the left module with the readout padboard removed and a complementary exploded view exposing the components of the right module. (right) Photograph of the eg6 RTPC during assembly.

the interaction of background particles which reduce efficiency of magnetic confinement of the low energy background. The tracking region will be formed by a two sets of light weight straws. The inner set of straws will hold a 2 mum gold plated kapton film. The outer set will be made of wires and used to increase the electrical field at a larger radius. To further minimize background events, a thin wall Be tube will be used for the first 50 cm of the beam line downstream from the target. After that a larger, standard Al pipe will provide connection to the exit beam line through the SBS magnet to the beam dump. The window between the low pressure, cold RTPC and atmosphere will be made from a pre-deformed 0.25 mm aluminum plate with a supporting grid of steel bars.

Each sub-assembly (window, cathode, three GEMs, and readout board) will be self-supporting and they will be nested together to form the detector assembly. The interior walls of the drift region will be printed-circuit-boards (PCB) patterned with metal traces forming the field cage. The axial PCB will extend above and below the active portion of the detector and will provide the high-voltage divider circuits and connection points, as well as pulse-injection circuitry for testing the electronics. By using a single GEM foil for a given GEM plane and using the cylindrical arrangement as in the BONUS and eg6 designs, the inactive azimuthal region of the detector can be reduced to an azimuthal region of 10°.

The RTPC is filled with an ionizable gas. During the BoNuS experiment a mixture of 80% helium and 20% dimethyl ether (DME) was used. To improve the energy loss dE/dx resolution inside the drift gas for the eg6 experiment, where recoiling helium nuclei had to be detected, the RTPC gas mixture was changed to 80% neon and 20% DME. Studies have shown that the later gas mixture has an improved resolution and hence we will use the neon-DME mixture for a cleaner separation of proton from pion and deuteron (plus
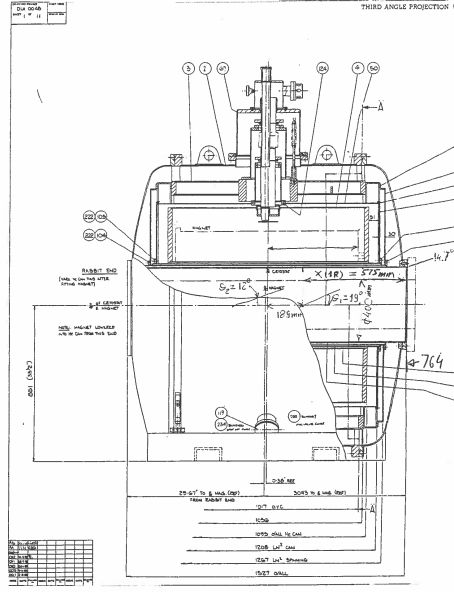
Figure 23: Technical drawing of the available solenoid.

heavier nuclei) background, and to extend the momentum acceptance, because of its high proton detection efficiency even at lower dE/dx.

Improvements in GEM electronics will allow for the readout cards to be placed at the two ends of the RTPC cylinder. This will allow some further increase in the drift region as compard to the BONUS and eg6 experiments by removing the need for radial on-board amplification. The outermost cylindrical layer of the detector will be the readout board made out of a flexible circuit board. The readout will be in a pad configuration with each pad having dimensions of 1 mm (azimuthal) x 21.25 mm (z). The pads will be connected by closed vias to traces on the outer surface of the readout board. The traces will connect to front end electronic cards located at the two ends of the cylindrical detector. All readout cards will be mounted parallel to the cylindrical surface, as illustrated in Fig. 24.

To readout signals from the detector, we will use the APV25 chip based Scalable Readout System (SRS) developed at CERN by the RD51 collaboration. The APV25 chip is an analog chip developed by the Imperial College London for the CMS experiment silicon trackers. It has been subsequently adopted by several experiments, such as the COMPASS trackers at CERN, STAR FGT at BNL and others. It is also palnned for the tracking detectors in the SBS project. The APV25 chip samples 128 channels in parallel at 20 MHz or 40 MHz and stores 192 analog samples, each covering 50 ns or 25 ns, per channel. Following a trigger, up to 30 consecutive samples from the buffer are read-out and transmitted to an ADC unit that de-multiplexes the data from the 128 channels and digitizes the analog information. Operating in the 20 MHz mode with the 30 sample readout will give a dynamic time range of 1.5 μs for the APV readout. This is sufficient to cover the drift time range of the TPC, which is expected to be approximately 1 μs
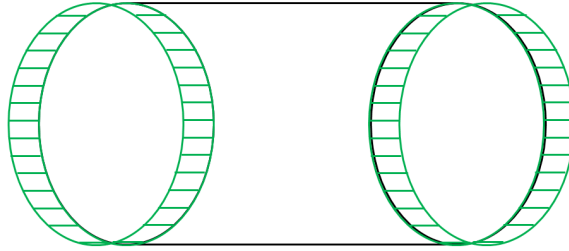
Figure 24: Schematic showing the SRS readout cards mounted at the two ends of the rTPC

corresponding to the increased drift velocity in the 0.1 atm RTPC gas mixture.

The SRS system is schematically shown in figure 25. It consists of the following components

- APV-25 hybrid cards mounted on the detector. These cards contain the 128 channel APV-25 chip which reads data from the detector, multiplexes the data, and transmits analog to the ADC card.

- SRS ADC unit that houses the ADC chips that de-multiplex data and convert into digital format.

- SRS FEC card which handles the clock and trigger synchronization. A single FEC and ADC card combination has the capability to read data from up to 16 APV hybrid cards.

- Scalable Readout Unit (SRU), an optional component not shown in the figure, which distributes the clock and trigger synchronization to the FEC cards. One SRU handles communication between multiple (up to 40) FEC cards and the data acquisition computer.

- The data acquisition computer, which could be part of a larger DAQ system as one of the readout controllers.

Work is currently underway to incorporate the SRS system into the CODA data acquisition framework at Jlab.

2.3.1   Target

The proposed TDIS target inside the RTPC is significantly different from those previously utilized. The target vessel is here a cylinder with an inner radius of 5 mm and 40 cm long. The target will be gaseous Hydrogen or Deuterium at 78k and 1.1 atm. In order
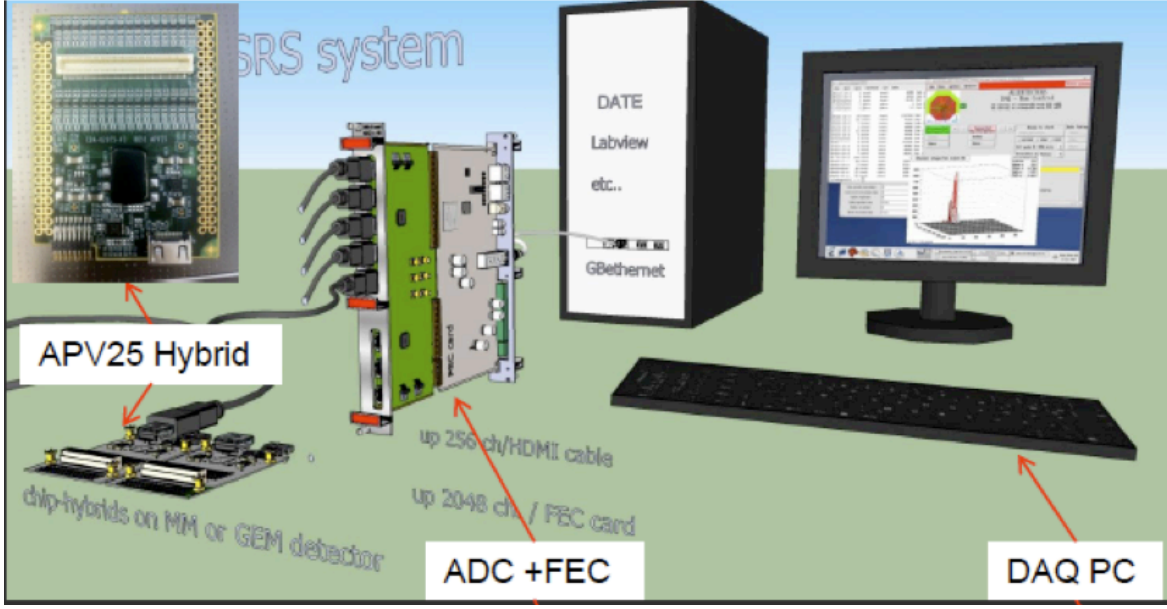
Figure 25: Schematic showing the SRS system

to minimize the energy loss of the protons of interest, we have reduced the material of the target wall as much as possible, down to 10 micrometers of aluminum. The larger diameter cell and aluminim walls are necessary given the 1000 times higher luminosity of the proposed experiment. The lower temperature of the target (liquid nitrogen level) and increased length of the cell allow reduction of the gas pressure in the target from 7 atm to 1 atm. The resulting threshold and energy loss for low energy protons are presented in Tab. **??**.

2.3.2   RTPC Calibration Using the HCAL Calorimeter

The proposed measurement of the tagged DIS cross section will require knowledge of the various detector acceptances and efficiencies. The fully inclusive electron-proton and electron-deuteron cross sections are well known from experiments in this kinematic regime at Jefferson Lab and SLAC [**?**]. Comparing our untaggged DIS measurements with these data will allow for precision checks of the acceptance, efficiency, and other corrections used for the SBS electron spectrometer analysis.

The RTPC will also require study and calibration. The BONUS experiment was not able to make precise acceptance and efficiency corrections to the RPTC data to measure the neutron cross section directly using the tagging technique, but rather had to simulate as well as normalize to a model F_2^n/F_2^d ratio for an assumed-known kinematics within the data set. This contributed significantly to the uncertainty of the measurement [84]. We could employ a similar approach, but suggest also that known quantities may be used as well to extract the RTPC acceptance and efficiency.

Some initial calibration can be done by using the copious proton tracks from elastic electron-proton scattering. At production luminosity there will be several accidental elastic proton tracks distributed evenly along the target for in every e-p DIS event. These protons are well separated from the protons of interest because, to be at the same momen-
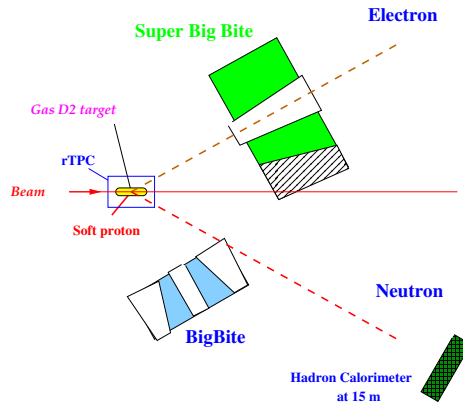
Figure 26: Setup for rTDC calibration

tum but generated by elastic events, they are necessarily kinematically directed almost perpendicular to the beam.

It will be particularly productive to use quasi-elastic electron scattering from the deuteron for the RTPC calibration. The energy and direction of the spectator protons can be calculated in the quasi-elastic reaction using only the scattered electron in the SBS in combination with neutrons measured with the SBS Hadron Calorimeter (HCAL). The moveable HCAL detector would not be a part of the SBS for this experiment, and could be placed beam right at optimum kinematics to record neutrons for this calibration measurement. In such a way we can predict the distribution of protons of energy 5-25 MeV (100-500 MeV/c) in the directions required for the RTPC calibration. A comparison between the measured proton spectra and the proton distributions expected in the RTPC from quasi-elastic neutrons in HCAL will provide a check on the RTPC proton acceptance and efficiency corrections. If the suggested quasi-elastic HCAL neutron measurement is for some reason not available to the proposed measurement, it will be possible to work through simulation and geometry as was done for these CLAS6 experiments.

The proposed calibration will be performed at a luminosity of 6×10^{36} Hz/cm^2 with an electron beam energy 2.2 GeV and SBS angle of 30 degrees. Projected rate of electron-neutron quasi-elastic events 10 kHz. The neutron momentum will be 1100 MeV/c. Using HCAL located at a distance of 15 meters (48 degrees relative to the beam) we estimated that the coincidence e-n rate will be approximately 1500 Hz. The angular resolution for the direction of the neutron momentum will be 3 milliradians. The time resolution of 0.5 ns will allow us to measure the total neutron momentum with an accuracy of 15 MeV/c. The proton momentum will be reconstructed to accuracy of 4 MeV/c for the components which are transverse to the direction of the neutron momentum.

2.4   The Super BigBite Spectrometer

The Super Bigbite Spectrometer (SBS), currently under construction and fully funded by DOE NP, consists of a dipole and a modular detector package. An important feature of
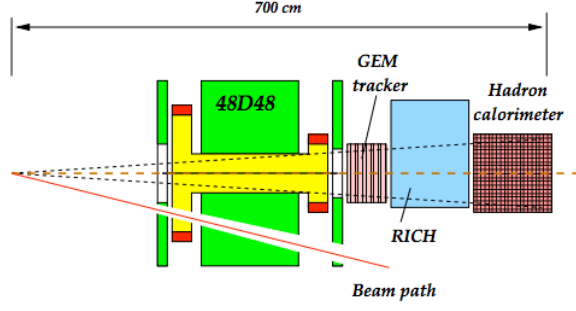
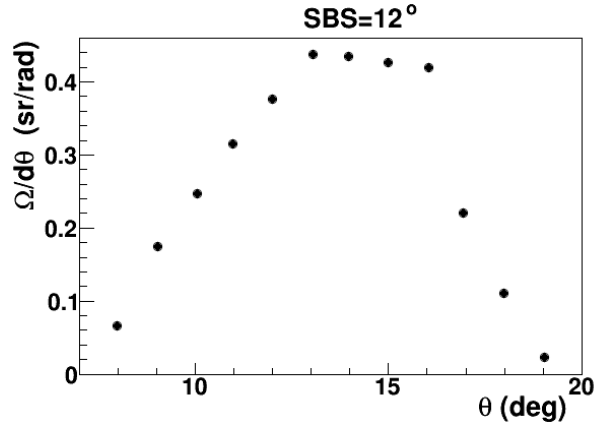Figure 27: Schematic of the Super Bigbite Spectrometer

Figure 28: The solid angle at 12 degree SBS position.

the SBS is a beam path through the opening in the right side yoke of the magnet, which allows it to be placed at forward angles as small as 3.5°. For the proposed experiment the SBS magnet (front face of the yoke) will be placed 2.0 m from the target allowing for a 50 msr solid angle around a 12 degree central angle. The large out-of-plane angle of SBS provides significant coverage in azimuthal angle (about 30% of 2π. Figure 28 shows the spectrometer solid angle vs. scattering angle for such a setting.

In the proposed experiment we plan to use the large GEM-based chambers currently under construction for the SBS G_E^p experiment polarimeter as electron tracking planes. We plan to use five out of ten constructed planes and concentrate the readout electronics of all ten planes in those five. These chambers will each cover a 60 cm x 200 cm area, and the concentrated electronics will then allow reading of every readout strip. These chambers were tested in such a configuration and a spatial resolution of 60-70 μm was obtained [?].

The combination of an electromagnetic calorimeter (previously the CLAS-6 Large Angle Calorimeter or LAC) and threshold gas Cherenkov counter (GC-SBS) will be used for trigger and particle identification purposes. The LAC is discussed in some detail below. The GC-SBS will be a straightforward modification of the existing ring imaging Cerenkov (RICH) detector planned to be utilized in the approved SBS experiment E12-09-018 - basically filling the tank with CO_2 gas rather than aerogel. The combination of these two detectors will be sufficient for the straightforward electron particle identification purposes

36

Electron arm – SuperBigbite
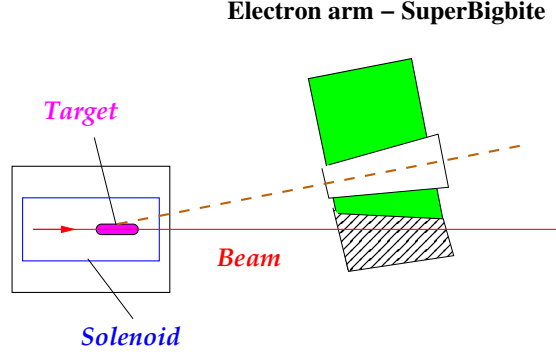
Target

Beam

Solenoid

Figure 29: Schematic layout of the proposed experiment.

of this experiment, mimicing that typically used in Jefferson Lab electron spectrometers. Moreover, the electron background coming from neutral pion production decaying into photons and subsequent electron-positron pairs is not expected to be an issue at the high momentum, small angle kinematics of this experiment. Figure 30 provides estimates of electron and pion production ratios obtained from the Wiser code [85] for a hydrogen target at 25k and 2 atm, similar to the conditions here proposed.

2.4.1 SuperBigBite Electron and Other Triggers

It is planned that the first level trigger will be formed using the total energy deposition in the LAC and the second level trigger will use correlation between the coordinates of the signals in the LAC and GC-SBS. The RTPC will be readout for any kind of trigger.

Pipelined Electronics For the SBS experiment Gep5 the proton trigger is achieved digitally using the Jefferson Lab Lab pipeline electronics. All of the 288 channels of the hadron calorimeter (HCAL) are continuously sampled at 250 MHz. The data of each block is sent to a crate trigger processor where the clustering algorithm computes the sums of 16 adjacent blocks and produces a trigger if one cluster is above threshold. This process takes about 700 ns. Once the trigger is generated, the data from the FADC is looked back up in the pipeline memory to be read out. Since the LAC has only 216 channels we propose to reuse the HCAL trigger electronics and readout to generate the single shower trigger. The singles shower trigger will also be prescaled in order to study the Cerenkov efficiency.

Large Angle Calorimeter The Large Angle Calorimeter is constituted of layers of scintillator and lead. For this experiment the sensitive area will be limited to 1.8m x 3.6m to match the SBS acceptance. The detector is arranged in two parts, the front part containing 16 layers and the back part containing 17 layers. This will correspond to a total number of 216 PMTs. With the geometry of the scintillators, the sum of all sets of 2 adjacent horizontal paddles and 2 adjacent vertical paddles will be computed and
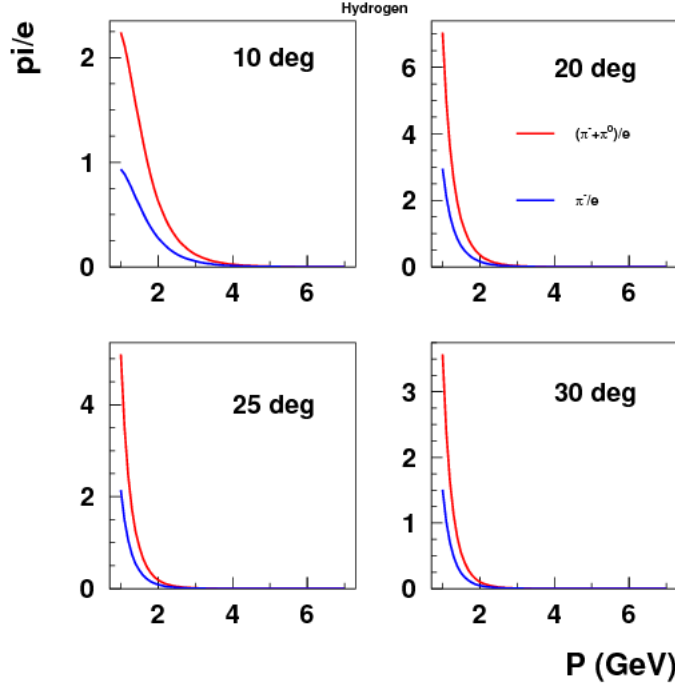
Figure 30: Estimates of pion to electron ratios for electron scattering angles as indicated, with negative and neutral pions combined in red and with negatively charged pions only in blue.

compared to the threshold.

Converted RICH Detector In order to reject pions and photons from the calorimeter trigger, we are planning to modify the RICH used for SBS transversity experiment by replacing the aerogel with CO_2 and using it as a threshold Cerenkov detector. The RICH is an array of 2000 PMTs. A 16 channel amplifier discriminator board was developed by Glasgow University based on the NINO Chip. Using discriminated signal provided by this board, with the amplitude over threshold of the signal integrated in the width of the logic signal, we would need 125 boards. A logic pipeline input register is being developed by the electronics group that can host up to 208 channels per board. We can reuse the second HCAL crate to hold the 10 input register boards of the RICH readout and generate an electron trigger by requiring the LAC electron trigger and a signal above threshold in the Cerenkov detector.

2.4.2 HCAL neutron detector

For SBS experiment Gep5, the electomagnetic calorimeter (ECAL) will also using summing modules. Since the HCAL has only 288 channels we propose to similarly sum and only use a subset of these electronics.

2.4.3 Readout

The readout of the SuperBigBite will be done using Flash ADCs for the LAC and input registers for the GC-SBS.

GEM Electronics The GEM signals will be read using the APV25 readout and the SRS system as described above. This will be used for the RTPC in the same way that it is currently planned for the GEM trackers of SuperBigBite.

Trigger number	Type
1	SBS LAC trigger
2	SBS LAC+Cer trigger
3	SBS and HCAL trigger

2.4.4 CLAS6 Large Acceptance Calorimeter

The SBS was originally designed to be a hadron spectrometer. In order to use it as an electron spectrometer we will (re)move the segmented hadron calorimeter to utilize it for calibration measurments as discussed above, and replace it in the SBS spectrometer with the safely salvaged Large Acceptance calorimeter (LAC) from the CLAS6 detector.

The conceptual drawing of the internal structure of the LAC is shown in Fig. 31. The LAC module has a rectangular shape with a sensitive area of 217 x 400 cm^2 and consists 33 layers, each composed of a 0.20 cm thick lead foil and 1.5 cm thick NE110A plastic scintillator bars. The total thickness is about 12.9 radiation lengths or 1 hadronic absorption length. Each scintillator layer is protected from contact with the lead by 0.02 cm thick Teflon foils. The width of the scintillators is roughly 10 cm and is slightly increasing from the inner layers toward the outer layers to provide a focusing geometry. Scintillators in consecutive layers are rotated by 90 degrees to form a 40 x 24 matrix of cells with area approximately 10 x 10 cm^2. The module is vertically divided into two groups: an inner (first 17 layers) and an outer (16 layers) groups. Each group has its own light readouts. Scintillators lying one on top of the other with the same orientation form a stack. The focusing geometry is such that any straight trajectory that originates from the target would hit two crossing stacks both in the inner part as well in the outer part. For each stack the light is collected at both ends separately using light guides coupled to EMI 9954A photomultiplier tubes. For each module there are 128 stacks and 256 photomultipliers [86].

The LAC energy resolution for electromagnetic showers is 7.5 ± 0.2 % [86]. Combined with CLAS, the pion contamination is less than 1% for cuts that give a detection efficiency of 95% for 2 GeV electrons [?].

A Geant4 simulation has been performed to study the LAC for this proposal. Fig. [32] shows the LAC in this Geant4 program. In this simulation we aimed to 1) optimize the number of layers that should be grouped into the inner part or the outer part; 2) establish the particle identification cuts for electrons; and 3) determine the pion rejection rate without combining any other detectors. Our results indicate that grouping the first 17 layers into the inner part should provide an optimal choice and that the particle identification be cut should include two parts: $E_{tot}/P > 0.33$ and E_{in} cuts. Here, E_{tot}/P is the fraction of energy deposited in the LAC compared to the total momentum of the particle, and E_{in} is the energy deposited in the inner layers only. The cut value for E_{in}
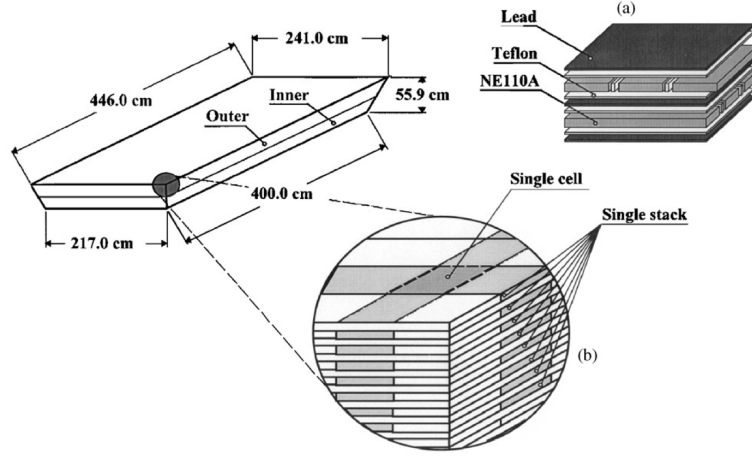
Figure 31: The conceptual drawing of the internal structure of the LAC module.

is mometum dependent. The results indicate that the pion rejection rates will be 89%, 92%, 95% and 96.5% for pions with momenta 1.0, 2.0, 5.0 and 8.0 GeV/c, respectively.

2.5 Simulations

2.5.1 Backgrounds

The impact of beam-related background processes on the RTPC has been assessed using a simulation based on the latest version of Geant-4 (4.10.0.p01). The simulation considers (Fig.33) a "straw" target of radius 5 mm and length 400 mm, held in a 10 μm thick Al cylinder, with 20 μm Be end windows, and filled with 2 atm of H_2 or D_2 gas. This is surrounded by the He gas of the RTPC, at a pressure of 0.05 atm (0.15 atm @ 77°K), contained within a volume of 150 mm radius. Both the straw target and the He volume are maintained at a temperature of 25°K or 77°K. A ring of 12.7 μm radius W field wires divides the He volume into an insensitive region (He-inner) at radii $r < 50$ mm and a sensitive region (He-outer) at radii $50 < r < 150$ mm. Ionization produced in He-outer is swept by the radial electric field to an outer ($r > 150$ mm) triple GEM detector with pixel readout.

Operating with the target at 25°K and 2 atm, an electron beam current of ~ 50 μA will produce a luminosity of 10^{37}cm^{-2}s^{-1}, reducing to 3.2×10^{36}cm^{-2}s^{-1} if the target is operated at 77°K. At these luminosities a large background will be generated in the vicinity of the target. This comes mainly from Mller scattering of the incident electrons, with smaller contributions from bremsstrahlung and pair production. Most of the background electrons have low energy and are confined inside the sensitive region of the RTPC by the solenoid magnetic field.

Fig. 34(A) shows the radial distribution for 5×10^7 incident electrons of energy deposited in the target and RTPC for different magnetic field strengths. The calculation has been made for uniform fields of 1.0, 2.0, and 4.0 T, as well as the "S3" solenoid field map (Fig.33) calculated in TOSCA. In the region of the target the maximum S3 longitudinal field is in excess of 4 T. As the field strength is increased the rate of decent of
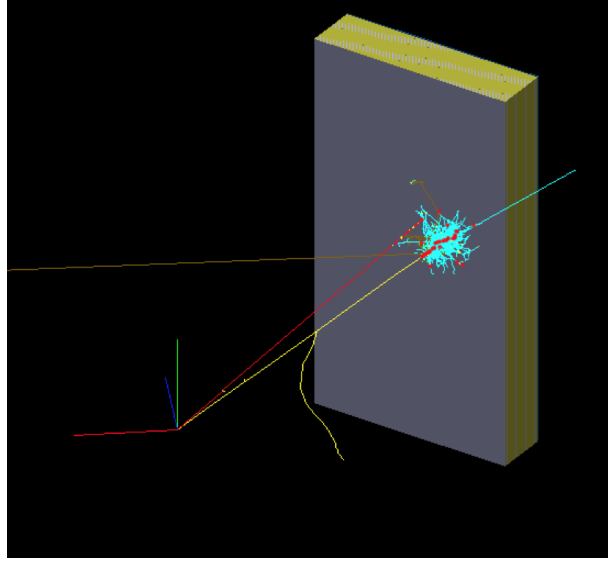
Figure 32: The LAC in the Geant4 Simulation. The red trajectory is a pion and the yellow is an electron.

Figure 33: Left: geometry of the MC simulation of background processes. Right: side view of the simulation geometry and the longitudinal component of magnetic field map S3
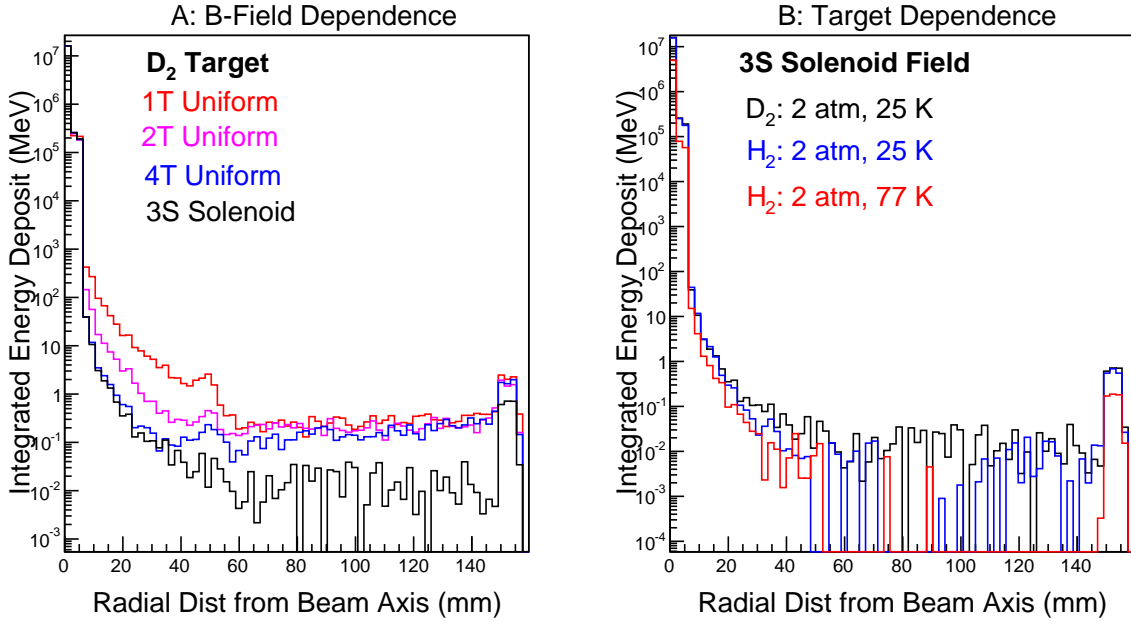

Figure 34: A: confinement of Møller energy deposit for a 2 atm, 25°K target and various magnetic field configurations. B: S3 solenoid field map and different targets. Simulations have 5×10^7 incident electrons of 11 GeV energy.

Target	Mean E_{dep} (MeV)	Mean E_{dep} (MeV)	Probability
	$r \leq 50$ mm	$50 < r \leq 150$ mm	
D_2, 25°K	0.33	0.41×10^{-7}	5×10^{-7}
H_2, 25°K	0.32	0.36×10^{-7}	3×10^{-7}
H_2, 77°K	0.10	0.11×10^{-7}	1×10^{-7}

Table 2: Electromagnetic background calculations for H_2 and D_2 targets operated at 2 atm pressure. The magnetic field is S3 solenoid.

energy loss, with respect to radius, becomes steeper in He-inner. However there remains a background in He-outer which is not suppressed by increasing the field strength. A small fraction, ~ 5 %, of this can be attributed to intermediate bremsstrahlung in the target region, followed by pair production. However most originates from interactions of the beam downstream from the target (Fig.33). It is thus important that the magnetic field extends well beyond the target and that the beam line has sufficiently large diameter to accommodate the increasing lateral spread in the exit beam. The present calculation has the exit beam line as stepped periodically to larger radii as one travels downstream from the target. Increasing the expansion of the exit beam line beyond that depicted in Fig.33 has an insignificant effect on the He-outer background if an electron beam radius of 0.5 mm is used. The integrated energy loss in He-outer has some dependence on the beam-line material, but 2-4 mm thickness Al gives reasonable results. Upstream from the target a dual W collimator is installed to suppress increased background produced by an off-axis beam. Fig. 34(B) shows the radial energy distribution, with the S3 field map and different 2 atm gas targets. The mean energy losses per incident 11 GeV electron are given in Table 2. Column "$r \leq 50$ mm" gives the mean energy loss in the target and He-inner and column "$50 < r \leq 150$ mm" the mean energy loss in He-outer.

The MC generated data have also been analyzed on an event-by-event basis and column "Probability" of Table 2 gives the probability of an electron event in the sensitive region where the mean dE/dx along the electron track exceeds 0.2 keV/mm. Protons of interest would be expected to produce a larger dE/dx. Taking for example the case of H_2 at 25°K, a 50 μA incident beam would produce a detectable rate of 9×10^7 Hz in the sensitive area. This would contribute to the occupancy of the readout pads in the GEM detector, but the electron track loci are quite different from those produced by protons.

Fig. 35 compares the transverse distribution of energy deposited for electrons (A) and protons (B). In A outside of the central region, there are ~ 5 tracks (equivalent to 10^{-7} probability per incident beam electron) which would reconstruct as originating from the target, with a radius of curvature consistent with $p \sim 250$ MeV/c and -ve charge. The outer ring of energy deposit is from photon conversion in the GEM detector. In B the photo proton tracks originate from the target region. For the deuterium target relatively large numbers of low momentum protons are produced as shown by the tightly curved tracks of radius a few cm.

Although electromagnetic processes are the dominant source of background, electrons impinging on the He-outer sensitive region generally have a relatively low energy loss, compared to the low-momentum protons of interest to recoil tagging. Photo nuclear processes, on the other hand, have much lower cross sections, but will produce significant
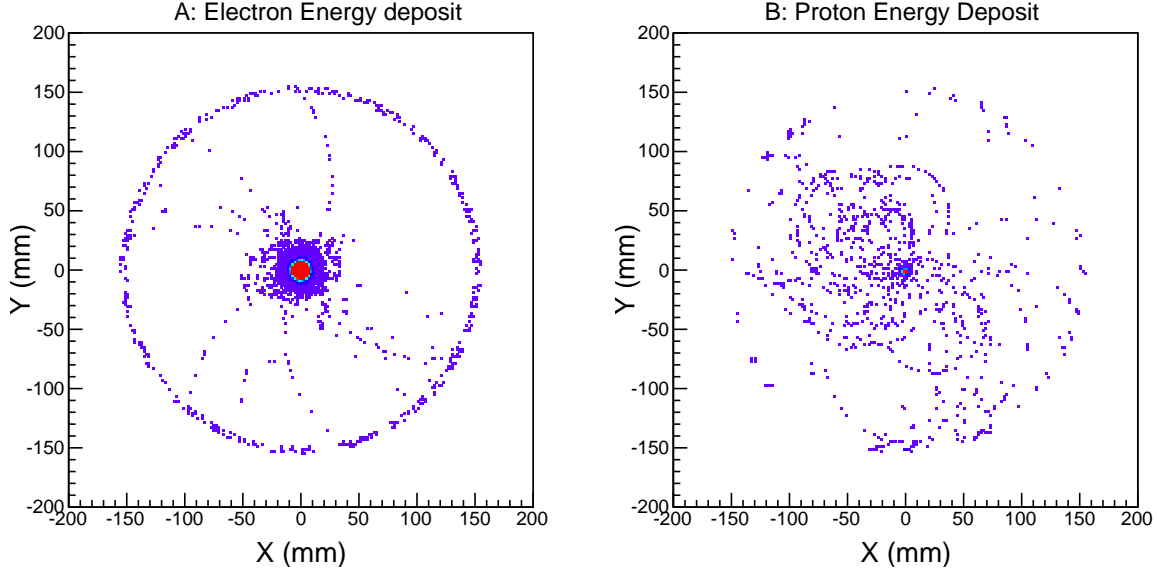
Figure 35: A: radial dependence of integrated energy loss for electrons, B: for photo protons.

Figure 36: Energy dependence of protons produced in the target by background photo nuclear processes. The targets are 2 atm, $25°$K, and the simulations ran 4×10^8 incident 11 GeV electrons.

numbers of highly-ionizing protons in a similar momentum range to those of interest. These protons will not be suppressed by the solenoidal field. Calculations have been made with the present simulation using the "extended electromagnetic" physics list of Geant-4 which includes photo- and electro-nuclear processes. Hadronic processes of produced nucleons and mesons are also included.

Fig. 36 compares the energy distributions of photo protons produced in the H_2 and D_2 targets. The number of generated photo protons and their distribution in energy is consistent with a calculation made by the DINREG code, which is based on Geant-3 and has been used previously to estimate the intensity of background processes in Hall A. Integrated over 4π, each incident 11 GeV electron has a probability of producing a photo proton of $\sim 10^{-6}$. The deuterium distribution has a much larger peak at low energy ($T_p \lesssim 20$ MeV) in the region of interest for tagged structure functions. This, and the different proton angular distributions from H_2 and D_2 has a major effect on the background which impinges on recoil-tagging kinematics.

Fig. 37 compares the angle and momentum of photo protons produced in H_2 and D_2 targets. The H_2 distribution is skewed to higher momenta (as in Fig. 36) and also to more forward angles. Thus cuts to select the recoil-tagging region of interest ($p_p < 250$ MeV/c, $35 < \theta_p < 80°$) have a much larger effect on the H_2 photo proton background rate. Table 3 shows the effect of applying such cuts, in terms of the probability of detecting a proton per incident 11 GeV electron.
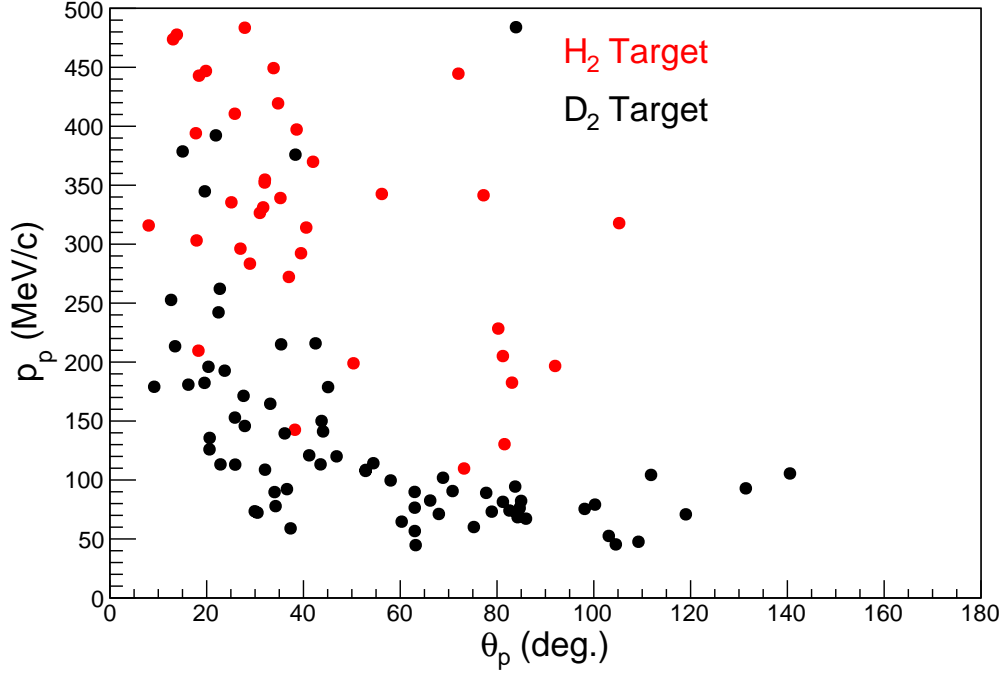
Figure 37: Comparison of momentum and angle dependence of photo protons produced in H_2 and D_2 targets and detected in He-outer. The targets were at 2 atm, 25°K, and the calculation is for 4×10^8 incident 11 GeV electrons.

40 cm Target 25°K, 2 atm	All produced protons	All protons $p_p < 250$ MeV/c	He-outer no cuts	He-outer $p_p < 250$ MeV/c	$p_p < 250$ MeV/c, $35 < \theta_p < 80°$
Hydrogen	9.8×10^{-7}	1.7×10^{-7}	1.1×10^{-7}	2.2×10^{-8}	8.0×10^{-9}
Deuterium	1.1×10^{-6}	6.3×10^{-7}	1.9×10^{-7}	1.6×10^{-7}	5.0×10^{-8}

Table 3: Photo proton production/detection probabilities per incident 11 GeV electron.

2.5.2 Kinematics

For the purpose of undertanding the kinematics of the experiment, electron scattering was generated in a simpler, basic Monte Carlo with a flat distribution in Q^2 from $1.0 - 10.0$ GeV^2, and a flat distribution in x_{Bj} from 0.001 to 0.5. The electron energy and angle are calculated and events are kept for electron angles between 5 and 45 degrees, and electron energies above 0.25 GeV.

The recoil proton was generated with a flat momentum distribution from 10 MeV to 400 MeV, a flat distribution in cos(theta) from 5 to 165 degrees, and a flat ϕ distribution across 2π. There is no explicit cut on transverse momentum p_T with respect to the photon direction. z is calculated as the ratio of the 4-momentum product of the recoil proton and photon to that of the initial proton and photon, so z is the 4-momentum fraction of the fluctuated proton longitudinal with the photon. z is required be between 0.8 and 0.98, so the accepted y_π values are from 0.02 to 0.2.

The splitting function is calculated as a function of y_π and p_T, and is required to be greater than zero. The t_π is required to be above -0.2 and below the proton t_{min} limit as defined above. x_π is defined as $x_{Bj}/(1-z)$, and is required to be between 0.0 and 0.99. Finally, the pion DIS cross section is calculated as a function of x_π and Q^2, neglecting off-shell effects, and using pion parton distributions in CERNLIB.

Fig. 38 depicts the electron scattering angle and energy range remaining after the cuts, and Fig. 39 depicts the recoil (target) proton momentum and angle range remaining after the cuts. It is important to note from the latter that the protons of interest to detect are in a range substantially less than 90 degrees. This is important, as the large background from elastic e-p scattering produces protons around a small cone 90 degrees from the scattering vertex. It will be possible to use reconstructed angle to separate the events of interest from those of the background. This will be more difficult for the deuterium measurment due to Fermi smearing.
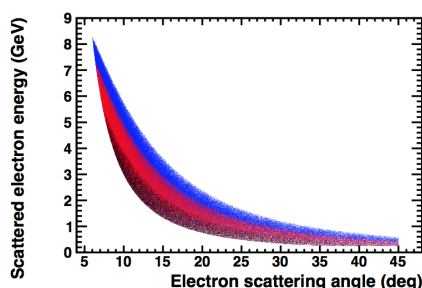

Figure 38: Scattered electron energy and angle dependence from the Monte Carlo.

A particularly nice result comes from looking at the projected data in t versus the pion momentum fraction y. In Fig. 40, the upper and lower red lines are the t_{min} for the Delta resonance, shifting the Delta mass by half the width. Here, the Particle Data Group estimate for the width of resonance of 118 MeV was used, and so the upper and lower lines correspond to +/-59 MeV. The central line represents the Delta mass, with the black data, then, below and the blue above the Delta. Plotting the data this way should
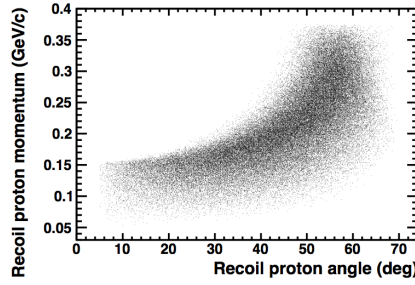
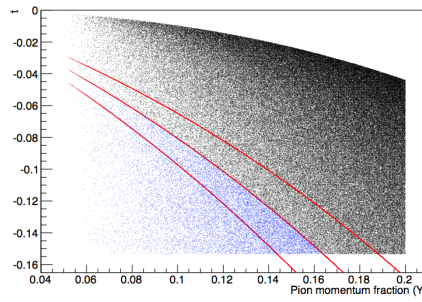Figure 39: Recoil proton momentum and angle dependence from the Monte Carlo.

Figure 40: Accepted counts in t versus the pion momentum fraction y. The black data are below the minimum t for the Delta resonance, and the blue are above. The red lines are the central value for the Delta, as well as the Delta mass shifted up and down by half the width.

allow for a kinematic cut to cleanly isolate events which could not have come from an intermediate Delta state in the low proton momentum range of interest for extrapolation to the pion pole.

3 Proposed Results

Sorry - still working and this section is short! But, here's the banner plot to consider....

Fig. 41, similar to Fig. 11 above, but with the projected data from this proposal added. For each x point, it is importnat to note that there will be four momentum bins also. This experiment will probe the mesonic content of the nucleon with high precision. The ratio of this content to the full nucleon cross section, the measured tagged to untagged ratio, is exactly the fracture function or the probability of finding the nucleon in a nucleon-meson state. While we will certainly utilize the momentum bins at each x to extrapolate to the pion pole, as well as the kinematic Delta resonance cut described above, to extract the pion structure function from these data, it is critical to point out that - regardless of the pion - this experiment will provide a direct measurement of the fracture functions.
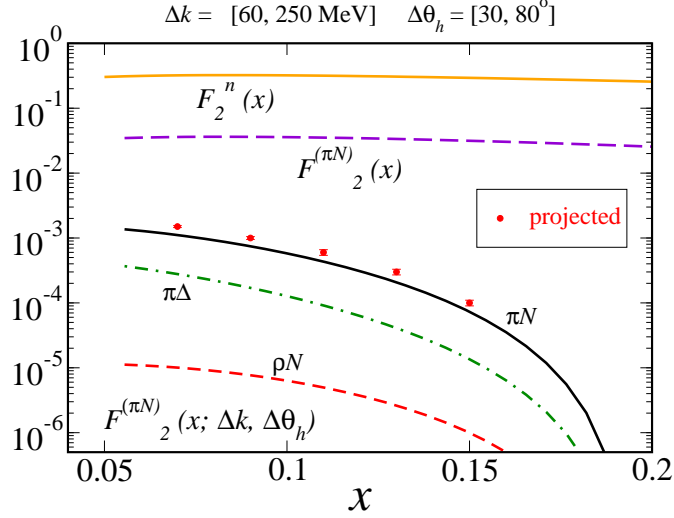
Figure 41:

3.1 Beam Time Estimate

We will request 10 days for hydrogen running, 5 days for deuterium running sacrificing the lowest cross section, highest x (y) point, and 5 days at reduced luminosity on hydrogen at that same high x, y point to verify the background subtraction, for a total of 20 days. This will be at a luminosity of 3×10^{36} cm^{-2}/s, achieved with 50 μAmps, and the target described above. The lower luminosoty runs will be obtained by running a lower (μAmp) current.

3.2 Expected Experimental Uncertainties

A systematic uncertainty of 5% was assumed, consistent with the BONUS experience utilizing the RTPC [84]. We need to add about the SBS, etc...

3.3 Applications to JLab 12 GeV Program and Beyond

Impact on GPD, TMD, SIDIS,...programs: for SIDIS, most experiments assume measurements of pi, k,... in the final state will provide important information on the hadronization mechanism - is this true if the target fragmentation (fracture function) is not well known?

Uncertainties in pi+/-p Drell-Yan (COMPASS) coming from large uncertainty in pion pdfs

New experiments, nuSEA, J-PARC, paving future for (m)EIC experiments,...

4 Summary

References

[1] Frisch and Stern, Zeits. f. Physik 85, 4 (1933); Estermann and Stern, Zeits. f. Physik 85, 17 (1933).

[2] E. Fermi, L. Marshall, Phys.Rev. 72 1139-1146 (1947).

[3] J.D. Sullivan, Phys. Rev. **D5**, 1732 (1972).

[4] J. Speth and A.W. Thomas, Adv. Nucl. Phys. 24, 83 (1997).

[5] P.L. McGaughey, J.M. Moss, and J.C. Peng, Ann. Rev. Nucl. Part. Sci. 49, 217 (1999).

[6] S. Kumano, Phys. Rep. 303, 183 (1998).

[7] A.W. Thomas, Phys. Lett. 126B, 97-100 (1983).

[8] V. R. Zoller, Z. Phys. C **53**, 443 (1992).

[9] W. Melnitchouk and A. W. Thomas, Phys. Rev. D **47**, 3794 (1993).

[10] H. Holtmann, A. Szczurek and J. Speth, Nucl. Phys. **A596**, 631 (1996).

[11] J. Speth and A. W. Thomas, Adv. Nucl. Phys. **24**, 83 (1998).

[12] S. Kumano, Phys. Rep. **303**, 183 (1998).

[13] W. Melnitchouk, A. W. Schreiber and A. W. Thomas, Phys. Rev. D **49**, 1183 (1994).

[14] R. Machleidt, K. Holinde and C. Elster, Phys. Rep. **149**, 1 (1987).

[15] B. Holzenkamp, K. Holinde and J. Speth, Nucl. Phys. **A500**, 485 (1989).

[16] D. de Florian and R. Sassot, Phys. Rev. D **56**, 426 (1997) [hep-ph/9703228].

[17] H. Holtmann, G. Levman, N. N. Nikolaev, A. Szczurek and J. Speth, Phys. Lett. B **338**, 393 (1995) [hep-ph/9602229].

[18] M. Glück, E. Reya, A. Vogt, Z. Phys. C **53**, 651 (1992).

[19] A. D. Martin, R. G. Roberts, W. J. Stirling and P. J. Sutton, Phys. Rev. D **45**, 2349 (1992).

[20] S. Kumano, Phys. Rept. **303**, 183 (1998) [hep-ph/9702367].

[21] G. T. Garvey and J. -C. Peng, Prog. Part. Nucl. Phys. **47**, 203 (2001) [nucl-ex/0109010].

[22] M. Gluck, E. Reya and A. Vogt, Eur. Phys. J. C **5**, 461 (1998) [hep-ph/9806404]; M. Gluck, P. Jimenez-Delgado and E. Reya, Eur. Phys. J. C **53**, 355 (2008) [arXiv:0709.0614 [hep-ph]].

[23] A. D. Martin, W. J. Stirling, R. S. Thorne and G. Watt, Eur. Phys. J. C **63**, 189 (2009) [arXiv:0901.0002 [hep-ph]].

[24] P. M. Nadolsky, H. -L. Lai, Q. -H. Cao, J. Huston, J. Pumplin, D. Stump, W. -K. Tung and C. -P. Yuan, Phys. Rev. D **78**, 013004 (2008) [arXiv:0802.0007 [hep-ph]].

[25] D. de Florian, R. Sassot, M. Stratmann and W. Vogelsang, Phys. Rev. D **80**, 034030 (2009) [arXiv:0904.3821 [hep-ph]].

[26] E. Leader, A. V. Sidorov and D. B. Stamenov, Phys. Rev. D **73**, 034023 (2006) [hep-ph/0512114].

[27] J. Dudek, R. Ent, R. Essig, K. S. Kumar, C. Meyer, R. D. McKeown, Z. E. Meziani and G. A. Miller *et al.*, *"Physics Opportunities with the 12 GeV Upgrade at Jefferson Lab,"* Eur. Phys. J. A **48**, 187 (2012) [arXiv:1208.1244 [hep-ex]].

[28] L. Trentadue and G. Veneziano, Phys. Lett. B323 201 (1994).

[29] J. C. Collins, Phys. Rev. D **57**, 3051 (1998) [Erratum-ibid. D **61**, 019902 (2000)] [hep-ph/9709499].

[30] G. Baum *et al.* [COMPASS Collaboration], *"COMPASS: A Proposal for a Common Muon and Proton Apparatus for Structure and Spectroscopy,"* CERN-SPSLC-96-14 (1996).

[31] F. D. Aaron *et al.* [H1 and ZEUS Collaborations], Eur. Phys. J. C **72**, 2175 (2012) [arXiv:1207.4864 [hep-ex]].

[32] F. D. Aaron, C. Alexa, V. Andreev, S. Backovic, A. Baghdasaryan, E. Barrelet, W. Bartel and K. Begzsuren *et al.*, Eur. Phys. J. C **71**, 1578 (2011) [arXiv:1010.1476 [hep-ex]].

[33] S. Chekanov *et al.* [ZEUS Collaboration], Nucl. Phys. B **816**, 1 (2009) [arXiv:0812.2003 [hep-ex]].

[34] F. D. Aaron *et al.* [H1 Collaboration], Eur. Phys. J. C **68**, 381 (2010) [arXiv:1001.0532 [hep-ex]].

[35] G. Altarelli and G. Parisi, Nucl. Phys. B126 298 (1977).

[36] ZEUS Collaboration, M. Derrick et al., Phys. Lett. B384 388 (1996).

[37] L. Trentadue and G. Veneziano, Phys. Lett. B323 201 (1994).

[38] D. de Florian and R. Sassot, Phys. Rev. D 56 426 (1997).

[39] H. Holtmann et al., Phys. Lett. B338 363 (1994).

[40] P. Maris, C. D. Roberts, P. C. Tandy, Phys. Lett. **B420**, 287 (1998).

[41] J. S. Conway *et al.*, Phys Rev. D **39**, 39 (1989).

[42] J. Badier *et al.*, Z. Phys. **C18**, 281 (1983).

[43] B. Betev *et al.*, Z. Phys. **C28**, 9 (1985).

[44] HI Collaboration, C. Adloff *et al.*, Eur. Phys. J. **C6**, 587 (1999); V. Andreev *et al.*, arxiv:1312.4821.

[45] G. R. Farrar and D. R. Jackson, Phys. Rev. lett. **35**, 1416 (1975).

[46] X. Ji, J.-P. Ma, and F. Yuan, Phys. Lett. **B610**, 247 (2005).

[47] S. J. Brodsky, M. Burkardt, and I. Schmidt, Nucl. Phys. **B441**, 197 (1995).

[48] M. B. Hecht, C. D. Roberts, and S. M. Schmidt, Phys. Rev. **C63**, 025213 (2001).

[49] P. Maris and C. D. Roberts, Int J. Mod. Phys. **E12**, 297 (2003).

[50] J. C. R. Bloch, C. D. Roberts, S. M. Schmidt, A. Bender, and M. R. Frank Phys Rev. **C60**, 062201 (1999).

[51] J. C. R. Bloch, C. D. Roberts, and S. M. Schmidt, Phys Rev. **C61**, 065207 (2000).

[52] T. Frederico and G. A. Miller, Phys. Rev, **D50**, 210 (1994).

[53] A. Szczepaniak, C.-R. Ji, and S. R. Cotanch, Phys. Rev. **D49**, 3466 (1994).

[54] T. Shigetani, K. Suzuki, and H. Toki, Phys. Lett. **B308**, 383 (1993).

[55] R. M. Davidson, and E. Ruiz Arriola, Phys. Lett. **B348**, 163 (1995).

[56] H. Weigel, E. Ruiz Arriola, and L. P. Gamberg, Nucl. Phys. **B560**, 383 (1999).

[57] W. Bentz, T. Hama, T. Matsuki, and K. Yazaki, Nucl. Phys. **A651**, 143 (1999).

[58] S. D. Drell, and T.-M. Yan, Phys. Rev. Lett **24**, 181 (1970).

[59] G. B. West, Phys. Rev. Lett. **24**, 1206 (1970).

[60] W. Melnitchouk, Eur. Phys. J. **A17**, 223 (2003).

[61] K. Suzuki and W. Weise, Nucl. Phys. **A634**, 141 (1998).

[62] J. D. Sullivan, Phys. Rev. **D 5**, 1732 (1972).

[63] A. Thomas, Phys. Lett. **B 126**, 97 (1983).

[64] NMC Collaboration, P. Amaudruz et al, Phys. Rev. Lett. **66**, 2712 (1991); P. Amaudruz *et al.*, Phys. Rev. **D 50**, R1 (1994)

[65] K. Gottfried, Phys. Rev. Lett. **18**, 1174 (1967).

[66] A. Baldit *et al*, Phys. Lett. **B 332**, 244 (1994).

[67] E866 Collaboration, E. A. Hawker *et al.*, Phys. Rev. Lett. **80**, 3715 (1998).

[68] E866 Collaboration, J. C. Peng *et al.*, Phys. Rev. **D 58**, 092004 (1998).

[69] E866 Collaboration, R. S. Towell *et al.*, Phys. Rev. **D 80**, 3715 (1998).

[70] HERMES Collaboration, K. Akerstaff *et al.*, Phys. Lett. **B 464**, 123 (1999).

[71]

[72] S. Kumano, Phys. Rep. **303**, 183 (1998).

[73] J. P. Speth and A. W. Thomas, Adv. Nucl. Phys. **24**, 83 (1998).

[74] G. T. Garvey and J. C Peng, Prog. Part. Nucl. Phys. **47**, 203 (2001).

[75] Nikolaev *et al.*, Phys. Rev. **D60**, 014004 (1999).

[76] B. Kopeliovich and B. Povh, Z. Phys. C **73**, 125 (1996).

[77] U. D' Alesio and H. J. Pirner Eur. Phys. J. A **7**, 109 (2000).

[78] V. Stoks Nucl. Phys. A **629**, 205c (1998);V. Stoks and Th. A. Rijken, Phys. Rev. C **59**, 3009 (1999).

[79] H. Hoffmann et al., Phys. Lett. **B 338**, 363 (1994).

[80] M. Gluck, E. Reya, A. Vogt, Z. Phys. **C 53**, 651 (1992).

[81] CERNLIB PDFLIB version 8.04.

[82] M. Gluck, E. Reya, A. Vogt, Z. Phys. **C 67**, 433 (1995).

[83] F. Sauli, Nucl. Instrum. Meth. **A386**, 531 (1997).

[84] S. Tkachenko *et al.* [CLAS Collaboration], Phys. Rev. C **89**, 045206 (2014).

[85] D.E. Wiser, Ph.D. Thesis, University of Wisconsin-Madison (1977) (unpublished).

[86] B. A. Mecking *et al.*, Nucl. Inst. and Meth. **A503**, 513 (2003).

[87] V. Sapunenko, *et al.*, Nucl. Instr. and Meth. A, to be submitted.